Chemistry with ADF

**G. TE VELDE,[1] F. M. BICKELHAUPT,[2] E. J. BAERENDS,[2]
C. FONSECA GUERRA,[2] S. J. A. VAN GISBERGEN,[3]
J. G. SNIJDERS,[4] T. ZIEGLER[5]**

[1]*Paragon Decision Technology BV, Julianastracit 30, Postbus 3277, NL-2001 DC Haarlem,
The Netherlands*
[2]*Theoretical Chemistry, Vrije Universiteit, De Boelelaan 1083, NL-1081 HV Amsterdam,
The Netherlands*
[3]*Scientific Computing & Modelling NV, Theoretical Chemistry, Vrije Universiteit,
De Boelelaan 1083, NL-1081 HV Amsterdam, The Netherlands*
[4]*Theoretical Chemistry, Materials Science Centre, Rijksuniversitet Groningen, Nijenborgh 4,
NL-9747 AG Groningen, The Netherlands*
[5]*Department of Chemistry, University of Calgary, 2500 University Drive NW, Calgary, Alberta,
Canada T2N 1N4*

ABSTRACT: We present the theoretical and technical foundations of the Amsterdam Density Functional (ADF) program with a survey of the characteristics of the code (numerical integration, density fitting for the Coulomb potential, and STO basis functions). Recent developments enhance the efficiency of ADF (e.g., parallelization, near order-N scaling, QM/MM) and its functionality (e.g., NMR chemical shifts, COSMO solvent effects, ZORA relativistic method, excitation energies, frequency-dependent (hyper)polarizabilities, atomic VDD charges). In the Applications section we discuss the physical model of the electronic structure and the chemical bond, i.e., the Kohn–Sham molecular orbital (MO) theory, and illustrate the power of the Kohn–Sham MO model in conjunction with the ADF-typical fragment approach to quantitatively understand and predict chemical phenomena. We review the "Activation-strain TS interaction" (ATS) model of chemical reactivity as a conceptual framework for understanding how activation barriers of various types of (competing) reaction mechanisms arise and how they may be controlled, for example, in organic chemistry or homogeneous catalysis. Finally, we include a brief discussion of exemplary applications in the field of biochemistry (structure and bonding of DNA) and of time-dependent density functional theory (TDDFT) to indicate how this development further reinforces the ADF tools for the analysis of chemical phenomena.   © 2001 John Wiley & Sons, Inc.   J Comput Chem 22: 931–967, 2001

Introduction

THE SUCCESS OF DENSITY FUNCTIONAL THEORY (DFT)

Kohn–Sham DFT[1–5] has in the recent past emerged as an important first-principles computational method[6–15] to predict chemical properties accurately[16–22] and to analyze and interpret these in convenient and simple chemical terms.[23–31]

The reasons for its popularity and success are easy to understand. In the first place, the DFT approach is in principle exact. The exact exchange-and-correlation (XC) functional is unknown, but the currently available XC functionals provide in most cases already a "chemical" accuracy of a few kcal/mol for binding energies.[16, 22, 32, 33] Moreover, the quest for more accurate ones based on a more detailed understanding of their essential properties is continuing.[27, 28, 34–46]

In the second place, it preserves at all levels of approximation the appealing one-electron molecular orbital (MO) view on chemical reactions and properties. The computed orbitals are suitable for the typical MO-theoretical analyses and interpretations.[27, 29–31] The KS method effectively incorporates all correlation effects.

In the third place, it is a relatively efficient computational method, and its fundamental scaling properties do not deteriorate when methodological precision is increased, in particular, when a more accurate XC functional is applied. Recent research paves the way to implementations that scale only linearly with the system size.[15, 47–60] This brings within reach the treatment by fundamental quantum chemical methods of systems with hundreds, maybe even thousands of atoms.

THE KOHN–SHAM MO MODEL

The basic postulate in Kohn–Sham DFT[61] is that we can apply a one-electron formulation to the system of N interacting electrons by introducing a suitable local potential $V_{XC}(\mathbf{r})$, in addition to any external potentials $V_{ext}(\mathbf{r})$ and the Coulomb potential of the electron cloud $V_C(\mathbf{r})$, and solving

$$\left(-\tfrac{1}{2}\nabla^2 + V_{ext}(\mathbf{r}) + V_C(\mathbf{r}) + V_{XC}(\mathbf{r})\right)\varphi_i(\mathbf{r}) = \varepsilon_i \phi_i(\mathbf{r}) \quad (1)$$

The potential V_{XC} is the functional derivative with respect to the density ρ of $E_{XC}[\rho]$, the exchange–and–correlation energy functional. The one-electron molecular orbitals (MOs) ϕ_i—with corresponding orbital energies ε_i—define the *exact* electronic charge density and give, in principle, access to all properties because these are expressible as functional of the density, in particular the energy. Moreover, they provide an intuitively appealing view of the system as being built from independent-electron orbitals with all ensuing interpretations.

The exact form of the exact energy density $E_{XC}(\mathbf{r})$, representing and incorporating all exchange and correlation (XC) effects is unknown. From general principles one can formulate conditions on what $E_{XC}(\mathbf{r})$ should look like, and several, more and more advanced expressions have been advocated for it in the literature. Their application to real systems has been impressively successful, and it seems likely that we are on the right track, and that a further increase of accuracy is a matter of time.

THE ADF PROGRAM

The Amsterdam Density Functional (ADF) program has been developed since the early seventies[6]—at that time named HFS, for Hartree–Fock–Slater—with the explicit purpose to exploit the DFT computational advantages. With later (and still ongoing) additions and improvements, notably by the Theoretical Chemistry research groups of Amsterdam[6, 11–15, 62–73] and Calgary[74–85] ADF has evolved into a state-of-the-art package for quantum-chemical research. This article is based on the ADF2000/2001 releases. Documentation, including user manuals and licensing and distribution information, is available at the Web site http://www.scm.com.

ADF supports a wide variety of exchange–correlation (XC) functionals (but no exact-exchange varieties that require the evaluation of multicenter integrals; see the Exchange–Correlation section for details), and incorporates relativistic effects with the ZORA formalism, in the scalar approach or with spin-orbit terms included. Basis sets are built with Slater-type orbital functions. The standard sets in the ADF database range from minimal

to triple-zeta-plus-double-polarization quality (and beyond, for some atoms). An easy-to-use utility program is provided to generate higher precision basis sets as required. Energy gradients and second derivatives (computed analytically) allow the computation of energy minima, transition states, reaction paths, and harmonic frequencies with IR intensities. Solvation and electric field environment effects can be taken into account, and the computable molecular properties include NMR chemical shifts, ESR, and various response properties using the time-dependent density functional theory (TDDFT): excitation energies, frequency-dependent (hyper)polarizablities, RAMAN intensities, and dispersion coefficients. Numerical precision is controlled by a flexible numerical integration scheme for the evaluation of integrals. QM/MM and linear scaling techniques are available for the treatment of very large systems, while parallelization speeds up the execution on multi-CPU systems.

The first part of this article—second and third sections—reviews the ADF implementation, regarding technical characteristics and functionality. The package is large, and the number of features steadily expanding. The scope and size of this article limit the amount of detail that can be shown in these sections, and some aspects will only be touched upon, if at all. In particular, the article does not include a discussion of the solid-state counterpart of ADF (BAND).[12, 86–88] The second part of the article is devoted to main themes in ADF from the outset, i.e., the analysis of chemical bonds and reactions and the development of tools and concepts that help achieve a deeper and more detailed understanding of electronic structures and reaction mechanisms. We elaborate upon these subjects in sections four–six on the chemical bond, chemical reactivity, and an application in the field of theoretical biochemistry (structure and bonding of DNA), while the seventh section contains an exemplary application of TDDFT.

To date, there has been no scientific publication that covers both the various methods and techniques in ADF (and the reason for particular choices made) and how they are applied, for all the many features in ADF together. We have found that many users of the ADF software see this as a "problem." By integrating methodology and chemical applications in the present article, we hope to fill the gap.

Part I. Implementation: Technical Characteristics

NUMERICAL INTEGRATION

All DFT implementations employ some kind of numerical integration scheme, because the mathematical expression for any relevant density functional makes an analytical integration of matrix elements of the XC potential between basis functions of whatever type impossible. ADF uses a Gaussian-type quadrature method[11, 12, 89] based on the partitioning of space in atomic cells. Each cell contains a core-region sphere, inside which the integrands with cusps and singularities at the nucleus are handled conveniently in spherical coordinates:

$$\int_{\text{cell}} f(\mathbf{r}) \, d\mathbf{r} = \int_{\text{sphere}} f(\mathbf{r}) \, d\mathbf{r} + \int_{\text{cell-without-sphere}} f(\mathbf{r}) \, d\mathbf{r} \quad (2)$$

$$\int_{\text{sphere}} f(\mathbf{r}) \, d\mathbf{r} = \int_0^R r^2 \, dr \int_0^{4\pi} f(r, \Omega) \, d\Omega \quad (3)$$

The Jacobian factor r^2 in eq. (3) removes the Coulomb singularity of the integrand at the nuclear position. The remaining cell-minus-sphere region is treated, after suitable coordinate transformations, by a Gaussian product formula in Cartesian-like coordinates.

The atomic cells fill all space "inside" the molecule. In the remaining "outer" region, farther away from the atoms, all integrands decay exponentially with the distance from the molecule are smooth, and do not have cusps. An accurate evaluation by numerical sampling techniques over that part of space is not very demanding.

The ADF numerical integration module automatically tunes the grid by varying the numbers of points in the different regions (atomic spheres, cells and the outer region), while monitoring a series of test integrals such that these are evaluated with an (input-adjustable) precision. This procedure has proven to be robust and reliable, and is able to produce any desired accuracy in the actual calculations. It is user-friendly, because one only has to specify the precision level, by a single parameter. At the same time it is flexible, as one can select any value from 0.5 (so inaccurate as to be almost meaningless) to 12.0 (effectively close to machine precision). Of course, a higher precision implies more points and a greater computational effort. As an indication of the scaling of computing time: increasing the precision

parameter by 1.0 will roughly double the number of grid points, and hence, the computing time. This is a crude estimate; much depends on the actual case.

ADF applies numerical integration not only to those integrals that cannot be done analytically, such as the matrix elements of the XC potential, but to most other integrals as well. This approach has two major advantages. In the first place, simplicity, and hence efficiency, as well as reduced chances of implementation errors. Numerical integrals, assuming that the grid itself is available, are easy for the developer to implement and for the computer to evaluate: straightforward do-loops and vector constructs. In the second place, it creates the freedom to select the types of basis functions that are intrinsically the most suitable for electronic structure calculations, but which might cause difficulties in analytical integration schemes, for instance Slater-type orbitals (STOs) or numerical atomic orbitals. It makes it almost trivial to implement the computation of all kinds of properties, as long as these are expressible as integrals over space of an integrand that one can evaluate without too much difficulty at an arbitrary point $\mathbf{r}$.

BASIS SETS

ADF exploits Slater-type functions (STOs) $f(\mathbf{r}) = Y_{lm}(\Omega)r^n e^{-\alpha r}$ as basis set elements, in terms of which the molecular orbitals (MOs) are expanded. The center of the function is at a nucleus, the Y_{lm} are spherical harmonics, and the exponential factor α determines the long-range decay of the function. In contrast to Gaussian-type orbitals (GTOs), used in many other quantum-chemical codes, STOs have the advantage of possessing the required cusp behavior as well as the appropriate long-range decay. This allows the construction of high-quality basis sets with relatively small numbers of functions. GTOs, in comparison, typically would need a factor of 3 more functions for the same level of basis set quality. (In practice, GTO schemes usually employ *contracted* basis sets, which, of course, reduce again the computational effort that the uncontracted set would require.)

The ADF package comprises a database with a large number of basis sets for all elements of the periodic table, ranging from minimum single-ζ (SZ) to doubly polarised triple-ζ (TZ2P) basis sets (http://www.scm.com). It incorporates special extended sets with very diffuse functions for (hyper)polarizability calculations,[67, 70–73] and others with very contracted deep-core function

sets for relativistic calculations within the ZORA formalism.[65, 66, 68, 69, 90] Easy-to-use tools are available to generate basis sets with any required accuracy, allowing (in principle) to approach the basis set limit and eliminate any inaccuracies resulting from basis set deficiencies. The implemented method is based upon even-tempered STO basis sets developed by Chong, similar to earlier work,[91] but with a few modifications that, for molecular properties, seem to give somewhat better results.

FROZEN CORE APPROXIMATION

An important aspect of ADF is the (optional) use of a frozen core to trim down the computational time by reducing the size of the variational basis set. Because deep-core atomic orbitals change very little upon bond formation, the frozen core approximation saves time without sacrificing much in quality. Use of frozen cores is preferred over pseudopotentials—which ADF does not support—because it is, in essence, an all-electron calculation. With a frozen core calculation you obtain the total charge density and potential in the valence *and* in the core region, ignoring only the slight *change* in the deep-core orbitals upon formation of the chemical bond.

To ensure orthogonality between the frozen core orbitals and the valence basis functions, the valence basis set used in the SCF equations is explicitly orthogonalized to the frozen core. This is achieved by adding to the valence set a series of auxiliary "core functions" χ_μ^{core}, precisely one for each frozen core *orbital*. Each valence function is replaced by a linear combination

$$\chi_\nu^{\text{valence}} \Rightarrow \chi_\nu^{\text{valence}} + \sum_\mu c_{\mu\nu} \chi_\mu^{\text{core}} \qquad (4)$$

The condition that each such modified valence function be orthogonal to each frozen core orbital determines exactly all the coefficients $c_{\mu\nu}$. The frozen core orbitals are taken from very accurate single-atom calculations with large STO basis sets. Note that the core functions do not add variational freedom to the (valence) basis set, and hence, do not increase the size of the secular (Fock) matrix to be diagonalized.

The ADF database offers for most atoms in the periodic table several basis sets with different "levels" of frozen core approximation, including all-electron basis sets to avoid the frozen core approximation altogether. The exact definition of the frozen core orbitals (expansion functions and coefficients) used with a basis set is stored in the corresponding database file.

SYMMETRY

ADF exploits molecular symmetry for analysis purposes and to enhance the computational efficiency. The latter applies in particular to numerical integrals, where only the integration over the symmetry-unique region in space has to be carried out (assuming that the integrands have been projected onto their totally symmetric component). The number of integration points is thereby reduced by a factor equal to the number of symmetry operators. Almost all of the commonly encountered point group symmetries that have real irreducible representations (irreps) have been implemented, including nonabelian point groups with up to an eight-fold symmetry axis. The program recognizes the symmetry automatically, but the user may specify to use a lower symmetry via input. Preparations have been made to extend the symmetry functionality to include all point group symmetries.

The Kohn–Sham–Fock matrix is constructed on the basis of functions that transform according to a particular irrep and subspecies of the point group. The symmetry-adapted functions are combinations of the original functions, orthogonalized on the frozen core as described earlier, and Löwdin orthonormalized among themselves, resulting in an orthonormal and symmetry-adapted basis set in which the Fock matrix is block-diagonal. Diagonalization—block by block—yields the MOs grouped by symmetry representation.

COULOMB POTENTIAL VIA CHARGE DENSITY FITTING

The analytical calculation of Coulomb matrix elements would require two-electron integrals with its characteristic n^4 scaling, leaving distance cutoffs aside. The involved four-center integrals, in the case of the physically appropriate STO basis functions, are far from trivial. Numerical integration, in combination with density *fitting*, greatly reduces the effort. The evaluation is simpler and the formal scaling is "only" n^3 rather than n^4.

Numerical Integration

With the exception of the Coulomb potential, all terms in the Kohn–Sham operator of eq. (1) are local in the sense that they can be evaluated readily as functions of $\mathbf{r}$. Rather than separately evaluating all Coulomb matrix elements, we first compute (see below) the value of the Coulomb *potential* $V_C(\mathbf{r})$ in each point $\mathbf{r}$ of the numerical integration grid. We then add $V_C(\mathbf{r})$ to the exchange–correlation potential

$V_{XC}(\mathbf{r})$ and any other (external) potentials and terms of the Fock operator and evaluate the Fock matrix elements by a single numerical integration, which we have to carry out anyway, namely for $V_{XC}(\mathbf{r})$.

$$F_{\mu\nu} \sum_k w_k \chi_\mu(\mathbf{r}_k) \left\{ -\frac{1}{2}\nabla^2 + V_{\text{Coulomb}}(\mathbf{r}_k) \right. $$
$$\left. + V_{XC}(\mathbf{r}_k) + \cdots \right\} \chi_\nu(\mathbf{r}_k) \quad (5)$$

The summation runs over all integration points $\mathbf{r}_k$. The only effort, apart from the trivial addition of $V_C(\mathbf{r})$ to $V_{XC}(\mathbf{r})$, lies therefore in computing the value of $V_C(\mathbf{r}_k)$.

Density Fitting

The density *fit* implies that the exact density, expressed as one- and two-center products of basis functions from the computed occupied MOs, is replaced by an expansion in one-center functions only.[6] The auxiliary "fit functions" are (also) STO-type functions, but different from the basis functions. In fact, for a single-atom calculation where all products of basis functions are one-center products, the perfect set of fit functions would include all *products* of basis functions. These fit functions are then not only *different* from the basis functions, but there are also *more* of them.

In molecules, the exact representation of two-center density terms by one-center expansions is practically impossible. A very accurate approximation is obtained, however, by taking a sufficiently large set of fit functions, and in particular, by adding "polarization" fit functions, i.e., STO-type fit functions with higher angular momentum quantum numbers. Practice has shown that this is an adequate and accurate approach. Moreover, the ADF utility program to generate basis sets with any required "completeness" accuracy can equally be applied to generate high-precision fit sets in case the existing fit sets may be found to be inadequate.

The density fit in ADF is performed on an atom-pair basis: the total density is partitioned in its distinct two-center (and one-center) components, and each atom-pair-density is fitted by fit functions on these two atoms only. As a result, the computational weight of the fitting procedure scales principally only as n^2 instead of n^3 (linear scaling techniques further reduce this). The possible benefit from using off-pair fit functions is heavily system dependent, and the fit sets would intrinsically be less robust and accurate if we relied on this. If we want to make sure that the fit quality is sustained independent of the actual system, the pair-wise fitting has to be

adequate in itself, and the use of off-pair functions becomes merely a computational burden.

The fit equation for the expansion coefficients c_i is

$$\rho_{\text{exact}}(\mathbf{r}) \approx \sum_i c_i f_i^{\text{fit}}(\mathbf{r}) \tag{6}$$

This is solved in a least-squared sense under the constraint that the number of electrons in the fit representation is preserved. Having obtained the approximate fit density approximation [eq. (6)], the corresponding Coulomb potential is

$$V_C^{\text{fit}}(\mathbf{r}) = \sum_i c_i f_i^c(\mathbf{r}) \tag{7}$$

For an STO-type fit function $f(\mathbf{r}) = Y_{lm}(\Omega) r^n e^{-\alpha r}$ the corresponding Coulomb potential function $f^c(\mathbf{r})$ is given by

$$
\begin{aligned}
f^c(\mathbf{r}) &\equiv \int d\mathbf{r}' \frac{f(\mathbf{r}')}{|\mathbf{r} - \mathbf{r}'|} \\
&= \int d\mathbf{r}' \, Y_{lm}(\Omega)(r')^n e^{-\alpha r'} \sum_{l'm'} \frac{4\pi}{2l'+1} \Psi_{l'm'}^*(\Omega') \frac{r_<^l}{r_>^{l+1}} \\
&= \frac{4\pi}{2l+1} \Psi_{lm}(\Omega) \int_0^\infty \frac{r_<^l}{r_>^{l+1}} (r')^{2+n} e^{-\alpha r'} \, dr' \\
&= \frac{4\pi}{2l+1} \Psi_{lm}(\Omega) \left\{ \frac{\int_0^r (r')^{n+l+2} e^{-\alpha r'} \, dr'}{r^{l+1}} \right. \\
&\qquad \left. + r^l \int_0^\infty (r')^{n-l+1} e^{-\alpha r'} \, dr' \right\} \tag{8}
\end{aligned}
$$

At large distances $\mathbf{r}$ a long-range multipole term dominates, which decays as q/r^{l+1}, where l is the angular momentum quantum number of the STO fit function, and q is the strength. For the $l = 0$ monopole function, q would be the total charge contained in the fit function, i.e., the integral over all space of the fit function itself. For small $\mathbf{r}$, the multipole term is modified by an exponentially decaying small-range term; at $\mathbf{r} = 0$, the function is zero.

The database files in the ADF package contain for each atom not only the basis functions (and the frozen core information) but also the fit functions centered on that atom.

SELF-CONSISTENT FIELD (SCF) PROCEDURE

The self-consistent solution of the Kohn–Sham equations is obtained in an iterative SCF procedure. From a trial density matrix P^k we compute the Fock matrix F^k and diagonalize it to obtain the eigenvectors, i.e., the MOs. The occupied MOs then yield a new trial density matrix P^{k+1}, etc., until P^k and P^{k+1} are identical, and we have reached self-consistency. Simply plugging the new P^{k+1} into the iterative procedure will often fail to converge and result in oscillatory behavior. Various methods exist to make the SCF converge, the simplest one being simple *damping*, in which P^k and P^{k+1} are averaged to determine a new P as trial density matrix. ADF employs the DIIS (direct inversion of the iterative subspace) method to obtain convergence.[92–95] This is a generalization of simple damping, taking the results of several previous cycles to construct a guess for the next cycle. With DIIS, it typically takes between 5 and 30 cycles to converge the SCF equations.

LARGE MOLECULES

DFT methods have, in principle, the same scaling behavior as Hartree–Fock (HF), namely n^4 when using two-electron integrals for the Coulomb potential matrix elements. Most implementations, however, scale formally as n^3 as a result of using either numerical integration or density fitting (or both) for handling the Coulomb potential. As a consequence, they are intrinsically much more efficient than correlated *ab initio* formalisms of higher-than-HF methodological accuracy (MP2, for instance). Nevertheless, even a (formal) n^3 scaling behavior makes the treatment of larger molecules a formidable task. Two approaches have emerged to deal with this problem, and most present-day codes exploit these to at least some extent, and display better scaling behavior as a result. In the first place, there has been an increasing effort, still continuing, to develop intrinsically order-n algorithms (linear scaling with system size). The idea is to exploit distance effects based on the notion that the interactions of a particular atom with other atoms in the molecule can be ignored, without significant loss of accuracy, for all atoms except those in its neighborhood. If we can somehow carry this consideration over to all aspects of the calculation we should arrive at a method where the effort per atom is limited by the maximum size of environment it chemically/physically "sees." This is intrinsically not system size dependent, so the total effort should scale linearly with the number of atoms.

In the second place, one may realize that in calculations on large systems we are usually only interested in a small active site where, say, the chemical bond is formed. The remaining part of the system must be included in the calculation, because leaving it out would remove relevant "boundary conditions"—typically: steric and electrostatic

effects—and thereby affect the outcomes too much. The *accurate* treatment of those outer parts, however, has often not much impact on the computed strength of the chemical bond, the energy profile of the reaction, etc. These outer parts of the system can, hence, be treated by much faster methods of lower methodological accuracy (molecular mechanics), in combination (QM/MM) with the accurate but more demanding quantum-mechanical methods for the crucial centre of the system.

Linear Scaling

The basic elements in a calculation that determine the computational effort and that increase with system size are (1) the numbers of basis and fit functions, and (2) the number of numerical integration grid points. Both aspects scale linearly with the system size. The number of fit functions is larger than the number of basis functions; up to a factor of 2 is quite common. The number of grid points is also proportional to the size of the system (number of atoms), but with an even much larger proportionality factor. For the analysis of scaling behavior such differences are irrelevant. We will, therefore, refer to these items only by the scaling properties, and denote each of the scaling numbers as n.

To obtain better-scaling algorithms, ADF applies locality properties[15] based on the common chemical reasoning that interatomic interactions over large distances in a molecule can be ignored, which is, in a sense, already reflected in the use of exponentially decaying atomcentered basis functions. To each basis and fit function one assigns a *range*, beyond which it is assumed negligible. The grid points are grouped together in small subsets ("blocks" of points), typically a few tens to a few hundred, that all lie in the same region of space. Each block is then associated with a certain location (center and extension) in space, and the function's range and the location of the block determine whether the function needs to be evaluated in that particular block.

Application of a yes-or-no cutoff, as an alternative to standard screening techniques, entails the risk of discontinuities in the energy surface. However, with stringent criteria this effect appears (so far) to be minor. The advantage of the cutoff approach is simplicity and a somewhat better performance improvement: the relevant data structure—the lists of atoms that are in each other's sphere of influence—can be computed in advance, and applied wherever needed.

Carrying these considerations through has the effect that (overlap, Fock, etc.) matrix elements between (basis, fit) functions are only computed when the functions' ranges overlap, while the actual evaluation of these integrals only addresses those blocks of points that fall in the range of both functions simultaneously. Many of the dominating aspects of a calculation are in this way reduced to algorithms that scale linearly. Of course, the system must be large enough to actually "see" the linear scaling behavior, and for some aspects the onset of the linear regime may become apparent only for fairly large molecules.

Analyzing all the steps in a calculation we find a large number of them that scale worse than linearly, and we would have to treat all of them to formally claim an order-n program. From a practical point of view, however, we need to deal only with the dominant aspects in calculations on systems that are of interest now and in the very near future, let's say up to a few hundreds, or maybe a thousand atoms. The ADF development project—still ongoing—to establish linear scaling has focussed first on the SCF procedure, which is concentrated around the construction and processing of the Fock matrix, and the TDDFT modules where the computational structure has many similar features. Other CPU-intensive steps, in the preparation before the SCF procedure can start, and in the postprocessing and computation of properties, have structural elements that are also very similar, and that will, hence, be amenable to the same treatment developed for the Fock matrix.

Within the SCF procedure two relatively important aspects have not been treated completely yet. First, the diagonalization of the Fock matrix scales as n^3 in the standard approach. At the moment, we have not yet tackled this aspect because the total time spent in diagonalization has not been dominant so far in ADF calculations. Second, the evaluation in the grid points of the multipole long-range components of the Coulomb potential is still an order-n^2 step because the $1/r$ type decay—not exponential—prohibits a short-range cutoff. Fortunately, processing of the multipole terms is not very demanding, but with increasing sizes of molecules this will sooner or later become significant, and this aspect is, therefore, a prime target for future efforts. Obviously, the structure of the multipole potential is suitable for tree-based fast multipole methods,[96] as all components are based on the fit functions expansions, which can be organized and grouped together per atom and per (l, m)-value. In ADF, we only need to evaluate the Coulomb potential in the integration points, instead of calculating Coulomb matrix elements directly. This will make the use of hierar-
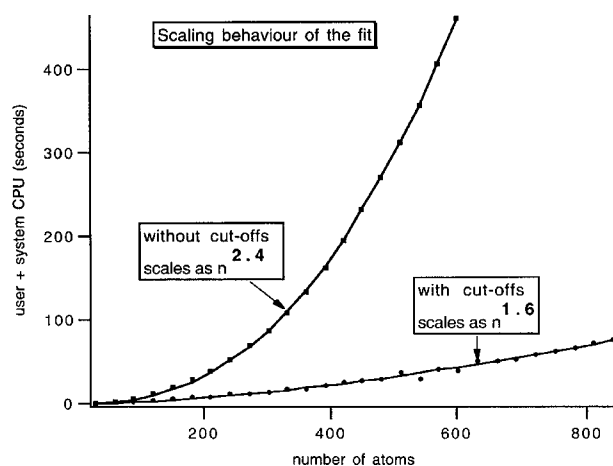
FIGURE 1. Scaling behavior of the fit procedure, that is, the calculation of fit coefficients, with and without distance effects.

FIGURE 3. Scaling behavior of the buildup of the Fock matrix, with and without distance effects.

chical multipole methods even simpler than when they have to be applied to the direct calculation of Coulomb matrix elements.

Figures 1, 2, and 3 display timing results—in the original and new implementation—for a systematic sequence of semi-one-dimensional alkanes, where the carbon atoms lie in a plane to form a regular seesaw chain and the hydrogen atoms are below and above the plane. In these systems the scaling improvements are exhibited most clearly due to their geometrical form where relatively many atoms are far apart. The scaling orders have been determined by fitting the results over the data range, so they represent only the *de facto* scaling over the range of used sizes, and will, generally speaking,
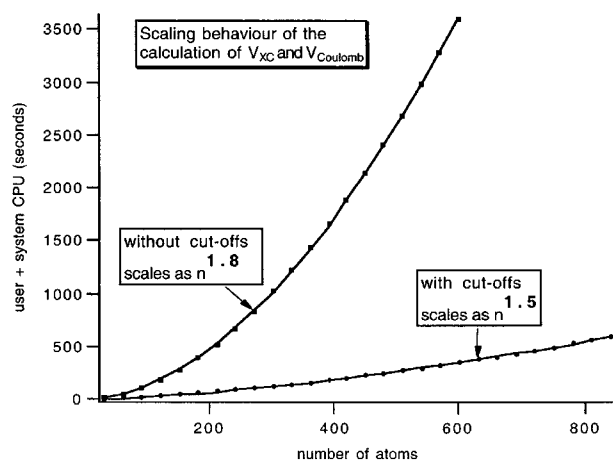

FIGURE 2. Scaling behavior of the evaluation of the (Coulomb and XC) potential in the numerical integration grid, with and without distance effects.
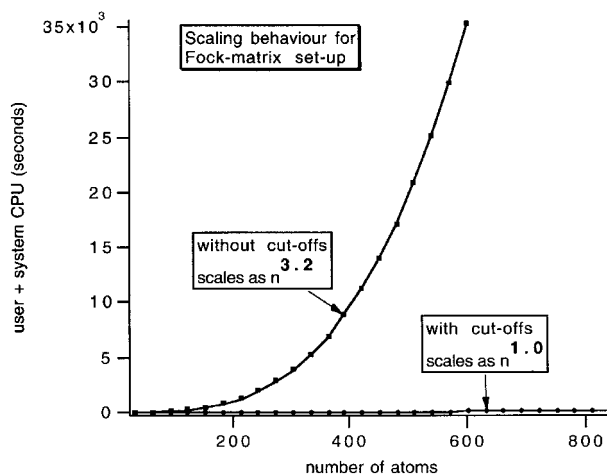
be just an effective average of underlying terms with different fundamental scaling behavior. The fit procedure (Fig. 1) does not show perfect linear scaling because of memory-cache and I/O effects that will have to be further analyzed. The result for the (Coulomb) potential in Figure 2, a scaling order of 1.5 instead of 1.0, is caused by the long-range multipolar term, which has not yet been treated, and hence, implies a term with scaling order 2. The Fock matrix setup—not including the computation of the potentials—scales perfectly linear.

With molecules of a few tens of atoms significant speed-ups are obtained by the implemented scaling techniques. The truly linear regime is seen in systems with hundred atoms and more.

QM/MM

The quantum mechanics—molecular mechanics (QM/MM) approach combines a "normal" (DFT) calculation on certain parts of the molecule or system with an approximate, force field-based method for the rest.[84, 85, 97] Typically, this is applied when one can partition a large system into a region that requires an accurate quantum mechanical description—the active site—and a remainder that acts only as a perturbation and can, therefore, be dealt with by approximate methods. The calculation proceeds in an iterative fashion. A pure-MM module optimizes the MM subsystem, taking the QM parts into account in the given QM geometry and considering the QM atoms as (frozen) MM atoms without information on the wave functions. Next, a QM calculation on the QM subsystem is performed including the (steric and electrostatic) ef-

fects from the MM part in the SCF procedure and the MM forces on the QM atoms in the geometry optimization step. With the new QM geometry the MM module takes control again, until convergence. The MM module uses a force field that is specified on a separate data file. Currently available in the ADF QM/MM procedure are AMBER95[98] and UFF[99] force fields. The setup is very modular, and other force fields can easily be inserted as additional options.

When the boundary between the QM and MM parts cuts one or more covalent bonds and the two subsystems are not well separated, the QM subsystem is defined with so-called "capping atoms." These are usually hydrogen atoms, and represent the MM part in the QM cycles of the computation. The "real" MM-atom that is bonded to the QM atom (and, hence, replaced by the capping atom in the QM calculations) is called the "link atom."

Various schemes have been advocated in the literature to combine the QM and MM calculations. They differ in their prescription for how the "true" bond between the QM-atom and the MM link atom is related to the pseudobond between the QM atom and the capping (hydrogen) atom. Most important approaches assume either or not a fixed *direction* from the QM system to the capping atom, and use either a fixed distance to the capping atom or a fixed ratio between the distance to the capping atom and the distance to the true MM atom. The ADF package supports three schemes: (1) the one originally proposed by Singh and Kollman;[100] (2) the approach of Maseras and Morokuma;[101] (3) a variation on the latter, using Cartesian rather than internal (Z-matrix) coordinates.[84]

In comparison with pure-QM calculations, even when these are highly optimized by linear-scaling techniques, the QM/MM approach is much more efficient. The MM contribution to the QM calculation cycles implies a small extra effort and the MM calculation cycles are very fast—depending somewhat on the chosen options. This is paid for by a reduced accuracy, or more appropriately formulated, by an additional uncertainty in the results. One needs to be sure that the partitioning has been adequate, and that not too much has been put into the MM approximation. Until sufficient expertise has been built up, this may imply that one has to perform additional validation calculations. Nevertheless, the QM/MM development clearly has paved the way to the treatment of much larger systems than were considered doable in a not too distant past.[102–105]

PARALLELIZATION

The implementation in ADF of parallelization[13] is based on the distributed-memory concept, using the single-program-multiple-data (SPMD) model. Although this may ignore some of the advantages of shared-memory architectures, it has the advantage that it can be applied generally. Shared-memory machines are treated as being of the distributed-memory type. For the parallel communication, PVM and MPI are both supported in ADF. Where we have to be specific in the following, PVM will be assumed for the sake of being concrete.

ADF is started on one of the nodes of the (virtual) parallel machine; this process is called the parent. The parent communicates with the system to create the child processes; it then reads the input and broadcasts this to the children. So, after the startup phase, a copy of ADF runs at each of the processes with exactly the same input data. In the serial (nonparallelized) parts of the program all these copies perform the same calculation, duplicating each other's work. In the parallel parts, each copy handles its share of the task and combines the results with the others. After all copies have finished the whole calculation, the child processes terminate, their private files are destroyed, and we are left with the results (output and other files) from the parent. A major advantage of the SPMD method is that the structure of the parallel program is virtually identical to the structure of the serial program. This makes it easier to maintain and develop both versions simultaneously. In fact, technically speaking, there are no separate parallel and serial versions at all.

General Approach

Communication between different processes is relatively time-consuming, and easily becomes a bottleneck in massively parallel runs. Minimization of communication is, therefore, crucial, even if at the expense of a slightly reduced balance of the workload distribution. Coarse-grained static load balancing keeps the communication times small: the data is kept local, and is not redistributed (static balancing) while communication is infrequent (coarse grain).

A general library has been developed for parallelization operations. All calling sequences to the procedures in the library are general, i.e., not specifically PVM or MPI or otherwise. The procedure interfaces are wrappers that contain PVM and MPI versions inside; the appropriate version is selected at compile time, when the human installer

chooses the message-passing method. This ensures that whatever is specific for the message-passing method is isolated in the library, and when new versions of PVM or MPI, or even completely new parallel facilities are to be used, changes have to be made only in this library.

Parallelization in ADF

The numerical integrations (matrix elements of the Fock operator, in particular) consume a major part of the CPU time in ADF. The number of integration points is typically of the order of a few thousands per atom. The points are partitioned in *blocks* of points, each block comprising a few tens up to a few hundred points. The blocks are distributed over the different processes, and each process stores on file only information related to its own blocks. Every numerical integral is implemented as an "outer" loop over the blocks, inside which the integral-specific work is performed, including an inner (vector-) loop over the grid points in that particular block. At the end of the loop-over-the-blocks the results from all processes are added. This approach has parallelized in a coarse-grain manner, yet very adequately, the numerical integrals and all related activities.

A second significant computational aspect of ADF is the determination of the density fit coefficients at each cycle of the SCF procedure, as a preliminary to the construction of the Coulomb potential. The procedure to compute the coefficients involves a loop over (all) pairs of atoms. This has been parallelized by distribution of the atom pairs over the parallel processes.

Performance

Not only the numerical integrals and the fit procedure have been parallelized but other, less CPU-intensive tasks as well. This has not been a redundant and only-academic effort. At first sight it may sound impressive when 90% or even 99% of the code runs perfectly in parallel, but such figures imply that the theoretical (maximum) speed-up is at most a factor of 10, respectively 100, even for extremely large numbers of nodes. This is expressed by Amdahl's law, which boils down to the simple fact that however many processes we assign to a task, we cannot reduce the time further than to what is spent in serial mode.

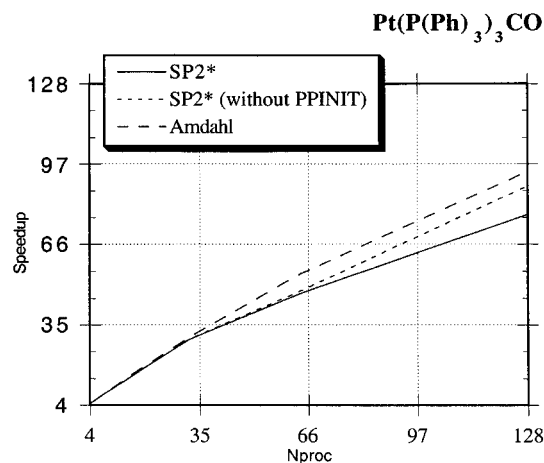$$T_n = t_s + \frac{t_p}{n} \tag{9}$$

FIGURE 4. Parallel performance of ADF. Displayed are the actual performance (obtained on an IBM SP2), the hypothetical performance without startup effort and the theoretically optimal performance given the fraction of the computation that runs in parallel mode (Amdahl's law).

t_s and t_p are the (elapsed) times of the serial and parallel parts of the code, respectively, when executed on a single processor. T_n is the time in an n-node run, assuming perfect load balancing and zero communication overhead.

The actual performance suffers not only from Amdahl's law. Imperfect load balancing, communication overhead, and startup times—the time spent in spawning the copies of the program before we can start computing—further degrade it. Startup times are sometimes ignored when presenting the successes of parallelization, but for the end-user only the true elapsed times count. Figure 4 presents the speedup for a (single-point) calculation on a $Pt(P(Ph)_3)_3CO$ complex. It also displays the prediction by Amdahl's law, based on timings performed in the ADF code to determine the serial and parallel parts of the calculation.

The fair correlation between Amdahl's law and the actual results implies that communication overhead and load imbalance are not yet severe at these numbers of parallel processes. Figure 4 also shows that a large part of the deterioration when more nodes are used is due to startup effects: routine PPINIT does little more than spawning the child processes.

Recent Developments

The very good load balance, implicit in the results shown in Figure 4 (from the parallelization project a few years back), relied on the fact that in the
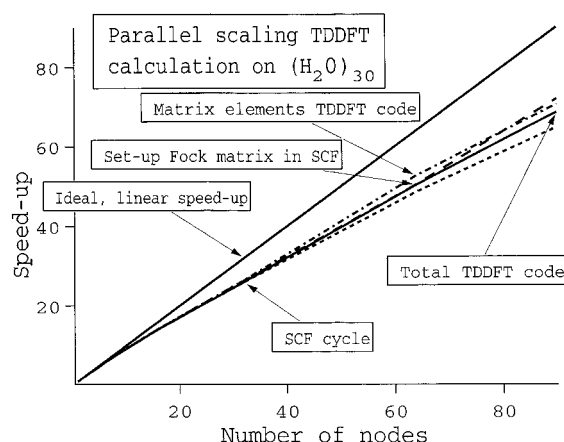
FIGURE 5. Parallel performance of ADF. Displayed are the parallelization speedups for the TDDFT module, and separately for the construction of the Fock matrix and the TDDFT matrix elements.

ADF version of that time each block of integration points carried almost exactly the same workload. Later developments changed that. The performance per block improved by linear scaling techniques, but not for each block to the same extent. A "work-load measurement" procedure, based on counting the numbers of basis and fit functions that are relevant for each individual block of points, has been applied to restore the load balance. Preliminary results for a few computationally dominant parts of the code (1-cycle SCF and 1-cycle TDDFT) demonstrate that this approach is successful: Figure 5 is based on timings with ADF2000 on a cluster of Pentiums.[106]

Functionality

ELECTRONIC STRUCTURE AND BONDING ANALYSIS

Fragment Approach

ADF builds a molecule from user-defined fragments, which may be single atoms or larger moieties, for example, ligands, functional groups, or complete molecules in a donor–acceptor complex. In practice, this means that the results of the ADF calculation on a fragment are saved on a file and that the fragment files are then used in setting up the calculation on the overall system. The fragment orbitals (FOs), i.e., the MOs from the calculations on the fragments, are employed as basis functions in the new calculation. This does not imply a basis set truncation or contraction because the virtual FOs are included: the FOs constitute

only a transformation of the basis set. If there are symmetry-equivalent fragments, for example, the six CO molecules in octahedral $Cr(CO)_6$, the program generates symmetry combinations of the FOs and uses the symmetrized fragment orbitals (SFOs) as basis functions. The SFOs transform as the irreducible representations (irreps) of the molecule, allowing a symmetry-driven analysis of the results. In absence of any symmetry the SFOs are identical to the FOs.

The fragment approach offers considerable advantages. It enhances the interpretative power of ADF as it leads to a more transparent picture of bonding, which reduces from a complicated mixing of many primitive basis functions (possessing little physical relevance) to a few key interactions between meaningful fragment (frontier) orbitals. This was already convincingly demonstrated in Extended Hückel studies,[107] and it also holds true for the Kohn–Sham DFT approach in ADF. The fragment approach also improves the numerical precision. In ADF, energies are calculated directly, *with respect to the fragments*, by *one single* numerical integral of the difference energy density $\varepsilon[\rho, \mathbf{r}] - \sum_A \varepsilon_A[\rho, \mathbf{r}]$ between the overall molecule and the constituting fragments.

$$\Delta E[\rho] = \int \left(\varepsilon[\rho, \mathbf{r}] - \sum_A \varepsilon_A[\rho, \mathbf{r}] \right) d\mathbf{r} \qquad (10)$$

In other words, we evaluate the energy of the overall molecule, $E[\rho] = \int \varepsilon[\rho, \mathbf{r}] d\mathbf{r}$, and the energies of each of the fragments, say the atoms that constitute the overall molecule, $E_A = \int \varepsilon_A[\rho, \mathbf{r}] d\mathbf{r}$, in *the same* numerical integration grid. This provides more accurate relative energies than subtracting total energies from separate calculations, because the same relative numerical integration error applies to a much smaller quantity, yielding, in turn, a much smaller absolute error.

Note that the user has the freedom to make his own choice of fragments. This is, however, not a matter of plain arbitrariness, and it does not make the analysis tools less meaningful. On the contrary, this freedom simply reflects the many perspectives from which a particular chemical phenomenon can be viewed.

In practice, many calculations are performed using as fragments the so-called *basic atoms*, which are the smallest possible building blocks in ADF. The basic atoms are not necessarily physically realistic objects—indeed, usually they are not, as they must be spin-restricted and spherically symmetric. The computed (bonding) energy w.r.t. basic atoms, then, does not yield quantities that can be compared

to experimental data directly. Rather, one must correct for the true ground state of the isolated single atoms.[108]

Bond Energy Analysis

In the framework of Kohn–Sham MO theory and in conjunction with the fragment approach, one can decompose the bond energy between the fragments of a molecular system—say, a base and a substrate for E2 elimination—into contributions associated with the various orbital and electrostatic interactions. In ADF, we follow a Mokokuma-type energy decomposition method.[23, 24, 31, 109, 110] The overall bond energy ΔE is divided into two major components [eq. (11)]. In the first place, the preparation energy ΔE_{prep} corresponding to the amount of energy required to deform the separated fragments, A and B say, from their equilibrium structure to the geometry they acquire in the overall molecule ($\Delta E_{prep,geo}$), and to excite them to their valence electronic configuration ($\Delta E_{prep,el}$). In the second place, the interaction energy ΔE_{int} between the prepared fragments.

$$\Delta E = \Delta E_{prep} + \Delta E_{int} = \Delta E_{prep,geo} + \Delta E_{prep,el} + \Delta E_{int}$$
(11)

In the following step, the interaction energy ΔE_{int} is further decomposed into three physically meaningful terms, which are printed in the ADF output file.

$$\Delta E_{int} = \Delta V_{elst} + \Delta E_{Pauli} + \Delta E_{oi} = \Delta E^0 + \Delta E_{oi} \quad (12)$$

The term ΔV_{elst} corresponds to the classical electrostatic interaction between the unperturbed charge distributions of the prepared fragments as they are brought together at their final positions, giving rise to an overall density that is simply a superposition of fragment densities $\rho_A + \rho_B$. (Note that we use the convention that energy terms containing potential energy only, kinetic energy only, or both kinetic and potential energy are indicated by V, T, and E, respectively.) For neutral fragments, ΔV_{elst} is usually attractive.[31, 111] The Pauli repulsion ΔE_{Pauli} arises as the energy change associated with going from $\rho_A + \rho_B$ the wave function $\Psi^0 = NA[\Psi_A \Psi_B]$ that properly obeys the Pauli principle through explicit antisymmetrization (A operator) and renormalization (N constant) of the product of fragment wave functions. It comprises the destabilizing interactions between occupied orbitals, and is responsible for any steric repulsion. In case of neutral fragments, it can be useful to combine ΔV_{elst} and ΔE_{Pauli} in a term ΔE^0 [eq. (12)] which, in the past, has been conceived as the steric interaction. However, we prefer to reserve the designation "steric" interaction or repulsion for ΔE_{Pauli} because that is, as already mentioned, the only source of net repulsive interactions between molecular fragments.[31] Finally, the wavefunction is allowed to relax from Ψ^0 to the fully converged wave function Ψ. The associated orbital interaction energy ΔE_{oi} accounts for electron pair bonding, charge transfer (e.g., HOMO–LUMO interactions) and polarization (empty/occupied orbital mixing on one fragment due to the presence of another fragment). This can be further decomposed into the contributions from the distinct irreducible representations Γ of the interacting system [eq. (13)] using the extended transition state method.[112] In systems with a clear σ/π separation, this symmetry partitioning proves to be very informative.

$$\Delta E_{oi} = \sum_{\Gamma} \Delta E_{oi,\Gamma} \qquad (13)$$

An extensive discussion of the physical meaning of all the terms in the energy decomposition is given in ref. 31.

Atomic Charges

Additional insight into bonding and reactivity can be gained if, complementary to the investigation of the wave function, one analyses the electronic charge density distribution. A convenient way to do so is by computing effective charges on the atoms in a molecule. In ADF, three different approaches are available for routinely computing atomic charges: (1) the Voronoi deformation density (VDD) method,[89, 113, 114] (2) the Hirshfeld scheme,[115, 116] and (3) the well-known Mulliken population analysis.[117, 118] Practice has shown that, despite its popularity, the latter is strongly basis set dependent. Hence, Mulliken charges are rather unreliable. We recommend the VDD and Hirshfeld atomic charges instead.

The VDD method is based on the *deformation* density and a rigorous partitioning of space into nonoverlapping atomic areas, the so-called Voronoi cells. The Voronoi cell of an atom A is the region in space closer to nucleus A than to any other nucleus (cf. Wigner–Seitz cells in crystals). The VDD charge of an atom A monitors the *flow* of charge into, or out of the atomic Voronoi cell as a result of "turning on" the chemical interactions between the atoms. The change upon going from the promolecule, in

which the density is the superposition of the initial, unperturbed atomic densities, to the converged SCF density of the molecule, is measured by:

$$Q_A^{VDD} = -\int_{\substack{\text{Voronoi} \\ \text{cell-}A}} \left(\rho(\mathbf{r}) - \sum_B \rho_B(\mathbf{r}) \right) d\mathbf{r}$$

$$= -\int_{\substack{\text{Voronoi} \\ \text{cell-}A}} \Delta\rho(\mathbf{r})_{\text{def}} \, d\mathbf{r} \qquad (14)$$

The VDD method summarises the three-dimensional deformation density $\Delta\rho_{\text{def}}$ on a per-atom basis [eq. (14)]. It is conceptually simple, and affords a transparent interpretation based on the plausible notion of charge redistribution due to chemical bonding, i.e., the gain or loss of charge in well-defined geometrical compartments of space.[89, 114, 119] See the Highly Polar Electron-Pair Bonding section for an application of the VDD method and a brief description of two recent extensions made in refs. 114 and 119.

The Hirshfeld charge of an atom A is defined as the integral of the SCF charge density weighted by the relative contribution, in each point in space, of the initial unperturbed charge density of that atom in comparison to the density of the promolecule already mentioned above, i.e., the superposition of the initial, unperturbed atomic densities:

$$Q_A^{\text{Hirshfeld}} = Z_A - \int \rho(\mathbf{r}) \frac{\rho_A(\mathbf{r})}{\sum_B \rho_B(\mathbf{r})} \, d\mathbf{r} \qquad (15)$$

One may interpret this as picking from the SCF density the parts that "belong" (according to the unperturbed densities) to the atom at hand. The current ADF implementation supports Hirshfeld (deformation) charges only with respect to the initial *fragments*, rather than to single atoms. The principle is the same, and in calculations that use single atoms as building fragments they are identical, of course.

The Voronoi deformation density (VDD) and Hirshfeld atomic charge of an atom A can both be written as the integral over *all space* of the *deformation* density times a weight function w_A^{Method} (Method = VDD, Hirshfeld).

$$Q_A^{\text{Method}} = -\int_{\substack{\text{all} \\ \text{space}}} \Delta\rho_{\text{def}}(\mathbf{r}) w_A^{\text{Method}}(\mathbf{r}) \, d\mathbf{r} \qquad (16a)$$

$$\begin{aligned} w_A^{VDD}(\mathbf{r}) &= 1 && \text{for } \mathbf{r} \in \text{ Voronoi cell } A \\ &= 0 && \text{for } \mathbf{r} \notin \text{ Voronoi cell } A \end{aligned} \qquad (16b)$$

$$w_A^{\text{Hirshfeld}}(\mathbf{r}) = \frac{\rho_A(\mathbf{r})}{\sum_B \rho_B(\mathbf{r})} \qquad (16c)$$

The atom-dependent weight function w_A^{Method} is either the hard-boundary Voronoi atomic cell [eq. (16b)] or the overlapping-initial-charge-distribution Hirshfeld "fuzzy cell" [eq. (16c)], respectively [in the latter case, one must only realize that Z_A in eq. (15) is equal to $\int \rho_A(\mathbf{r}) \, d\mathbf{r}$]. The VDD and Hirshfeld charges are evaluated by numerical integration in ADF, and both appear to be rather reliable. They match each other reasonably well, are not very sensitive to basis set effects, and their outcomes conform much better to chemical intuition than Mulliken charges do.[113, 114]

It may be noted here that, although the VDD and Hirshfeld atomic charges conform in practice rather well to common chemical reasoning, atomic charges in general, by whatever method defined, have an element of arbitrariness. Atomic charges are meaningful primarily in the comparison of trends where any arbitrariness in the definition of the charges is eliminated or at least strongly reduced.

EXCHANGE–CORRELATION (XC) FUNCTIONALS

To calculate the self-consistent solutions of the Kohn–Sham equation the exchange–correlation (XC) potential V_{XC} is derived from an approximate expression E_{XC} for the exact XC energy. Various approximations have been implemented in ADF, at the level of the local density approximation (LDA), and with corrections from the generalized gradient approximation (GGA) included. At the LDA level pure-exchange, or Slater's Xα parameterization can be chosen, or the Vosko–Wilk–Nusair (VWN) parameterization of electron gas data.[120, 121] The latter effectively includes correlation effects. Optionally, this may further be modified with the correction for the correlation between like-spin electrons as proposed by Stoll.[122] At the GGA level, the first implemented options included the formulas of Becke (exchange), Perdew (correlation), Perdew–Wang (both), Lee–Yang–Parr (correlation).[123–126]

The fundamentals of density functionals and their essential characteristics are a subject of ongoing research. Development of the Van Leeuwen–Baerends potential (LB94)[34] targeted the long-range behavior of the XC potential and indeed improved properties that critically depend on the long-range behavior such as (hyper)polarizabilities and high-lying excitation energies. This has been further improved upon by the orbital-dependent SAOP (statistical average of orbital potentials), which have yielded very good results for response properties.[127, 128] Research on this subject is continuing, and new XC potentials are being developed.[129] Recently published energy XC functionals devel-

oped elsewhere, such as the meta-GGA by Perdew and coworkers,[40, 41] have been implemented as well.

The available functionals do not include B3LYP and other "exact exchange" functionals when these require multicenter integrals, because their computation would affect the computational advantage of the DFT technology too much. The newer (pure DFT) functionals seem to be at least competitive in accuracy.

RELATIVISTIC EFFECTS

ADF supports the incorporation of relativistic effects by the quasi-relativistic method based on the Pauli Hamiltonian[63, 64, 130–137] or the more recently developed zero-order regular approximation (ZORA).[65, 66, 68, 69, 90] The Pauli Hamiltonian containing the first-order relativistic correction terms (Darwin, mass-velocity and spin-orbit coupling) presents a fundamental problem as it is not bounded from below. A large part of the relativistic effects can be accounted for by the first-order perturbation theoretic scheme if the first-order corrections to the density are taken into account ("coupled").[63, 64] In frozen core calculations one observes a considerable improvement over the coupled first-order perturbation treatment when the Pauli Hamiltonian is diagonalized in a restricted space consisting of just the valence (occupied and virtual) orbitals from conventionally used double-zeta and triple-zeta STO basis sets. This holds especially for very heavy elements like actinides.[135] [See ref. 136 for an extensive discussion and documentation, in particular for metal–ligand bond energies.] The diagonalization of the Pauli Hamiltonian is usually denoted as the quasi-relativistic method.[138] For the quasi-relativistic method it is essential that the frozen core approximation be used *and* that the valence basis is limited, to avoid a variational collapse. Indeed, it is sometimes found, to the dismay of users that are not fully aware of this aspect, that their Pauli relativistic calculations give worse results when they apply bigger ("more accurate") basis sets and/or relax the frozen core.

The ZORA method is generally found to give a more accurate description of the relativistic effects. It also avoids the problems in the Pauli formalism arising from the singular nature of the Coulomb potential, thereby eliminating the above-mentioned counterintuitive considerations of the basis set as-

pect in a calculation. The ZORA formalism is the recommended method in ADF.

The relativistic calculation is very similar in structure to a nonrelativistic one, having only a few additional terms in the Hamiltonian.

Pauli Formalism

In the Pauli formalism relativistic effects are included to first order in $1/c^2$, where c is the velocity of light. The Pauli Hamiltonian has relativistic terms given by

$$H_{\text{Pauli}} = -\frac{p^4}{8m^3c^2} + \frac{\nabla^2 V}{8mc^2} + \frac{1}{4mc^2}\sigma \cdot (\nabla V \times \mathbf{p})$$
$$\equiv H_{MV} + H_D + H_{SO} \qquad (17)$$

The mass-velocity term H_{MV} describes the relativistic increase of electron mass with velocity, and can be considered a correction to the nonrelativistic kinetic energy. Its matrix elements are

$$\langle \chi_i | H_{MV} | \chi_j \rangle = -\frac{\alpha^2}{8}\langle \nabla^2 \chi_i | \nabla^2 \chi_j \rangle \qquad (18)$$

The Darwin term H_D is the nonclassical contribution of the so-called *Zitterbewegung*, i.e., the quantum-mechanical effect associated with rapid movements of electrons around their average positions, and can be considered the correction to the nonrelativistic potential. The matrix elements are

$$\langle \chi_i | H_D | \chi_j \rangle = \frac{\alpha^2}{8}\Big[\langle \nabla^2 \chi_i | V | \chi_j \rangle + \langle \chi_i | V | \nabla^2 \chi_j \rangle$$
$$+ 2\sum_k \langle \nabla_k \chi_i | V | \nabla_k \chi_j \rangle \Big] \qquad (19)$$

$\alpha = e^2/(4\pi\varepsilon_0\hbar c)$ is the fine structure constant, H_{MV} and H_D are the *scalar* relativistic terms. Their matrix elements have the same symmetry as the nonrelativistic Fock operator. The extra effort they bring along is the calculation of the gradients of the orbitals in the integration grid; the Laplacian has to be calculated anyway for the nonrelativistic kinetic energy.

Spin-Orbit Coupling

The spin-orbit term H_{SO} results from the interaction of the electron magnetic moments with the magnetic field generated by their own orbital motion. The computation becomes more involved now than for the scalar relativistic terms because the spin-orbit term does not have the ordinary molecular symmetry. Instead, it is invariant under the

molecular point *double* group, which affects both spin and spatial coordinates. From the orbitals (or basis functions) that are adapted to the irreps of the ordinary point group we obtain the spin orbitals adapted to the double group by coupling the space and spin parts with the (double group) Clebsch–Gordan coefficients.

$$\chi_{\Delta\mu}(\mathbf{r},s) = \sum_{\alpha p} \chi_{\Gamma\alpha}(\mathbf{r})\eta_p(s)\langle\Gamma\alpha\Gamma_s p|\Delta\mu\rangle \quad (20)$$

$\eta_p(s)$ are the primitive spin functions ($\eta_1 = \alpha$, $\eta_2 = \beta$) and Γ_s is the double group representation spanned by these spin functions. The coupled functions are now adapted to the irrep Δ of the double group. The spin-orbit matrix elements for these functions are

$$\langle\chi_{\Delta\mu r}^{\Gamma_1}|H_{SO}|\chi_{\Delta\mu s}^{\Gamma_2}\rangle = \sum_{i\alpha\beta} B_i(\Delta\mu|\Gamma_1\alpha\Gamma_2\beta)$$

$$\times \langle\chi\Gamma_1\alpha r|\Omega_i|\chi\Gamma_2\beta s\rangle \quad (21)$$

We have separated the space and spin part here, given by

$$\langle\chi\Gamma_1\alpha r|\Omega_i|\chi\Gamma_2\beta_s\rangle = i\frac{\alpha^2}{4}\sum_{jk}\varepsilon_{ijk}\langle\nabla_j\chi\Gamma_1\alpha r|V|\nabla_k\chi\Gamma_2\beta_s\rangle$$

$$(22)$$

$$B_i(\Delta\mu|\Gamma_1\alpha\Gamma_2\beta) = \sum_{pq}\langle\Delta\mu|\Gamma_1\alpha\Gamma_s p\rangle(\sigma_i)_{pq}\langle\Delta\mu|\Gamma_2\beta\Gamma_s q\rangle$$

$$(23)$$

ε_{ijk} is the totally antisymmetric Levi–Civita tensor; $(\sigma_i)_{pq}$ are the Pauli spin matrices. The Clebsch–Gordan coefficients $\langle\Delta\mu|\Gamma_1\alpha\Gamma_s p\rangle$ can be calculated from the irreps of the double group.

Spin-orbit effects can usually be ignored for bonding energies and geometry minimizations of closed shell molecules. The complete calculation can then be done with the ordinary (single) point group using only the scalar relativistic terms. The current implementation does not support geometry optimization with spin-orbit terms included.

ZORA

The ZORA method is obtained by rewriting the energy expression and expanding in the parameter $E/(2mc^2 - V)$, which remains small even close to the nucleus. Retaining only the zeroth order term we get

$$E = \frac{p^2c^2}{2mc^2 - V} + V \quad (24)$$

The ZORA Hamiltonian reads

$$\begin{aligned}H_{ZORA} &= \sigma\cdot\mathbf{p}\frac{c^2}{2mc^2 - V}\sigma\cdot\mathbf{p} + V \\ &= \sum_i p_i\frac{c^2}{2mc^2 - V}p_i \\ &+ \frac{mc^2}{(2mc^2 - V)^2}\sigma\cdot(\nabla V\times\mathbf{p}) + V \quad (25)\end{aligned}$$

Again, this can be written as a sum of terms that have the (single group) symmetry of the molecule and a spin-orbit term that is invariant under the double group.

SOLVENT EFFECTS: COSMO

The conductor-like screening model (COS-MO)[139–141] has been implemented in ADF[83] to include solvent effects for reactions and material properties in solution rather than in the gas phase or the solid state. In this method the environment effects are treated in an approximate fashion. The solvent is handled as a dielectric medium that induces charge polarisation on a suitably defined surface around the molecule—the cavity—immersed in the solution. Any detailed properties of the solvent are reduced to an assumed rigid sphere size of the solvent molecules, which aspect is only used to determine how far the solvent can penetrate into the region occupied by the molecule. This thereby plays a role to determine the effective molecular surface, the solvent accessible surface (SAS).

Technically the SAS is defined as the envelope of a series of spheres.[139, 142, 143] These are atom-centered spheres with Van der Waals-type radii (a bit larger, usually, than standard Van der Waals radii), augmented by auxiliary spheres, if necessary, to describe the effective cavity that contains the molecule and that is not accessible for the solvent.

The surface-describing spheres are partitioned, typically in 60 surface triangles, and each triangle is assigned a point charge, the strength of which is adjustable. Because the spheres defining the SAS may intersect, only those triangles are used that are actually on the surface of the molecule and not, for instance, inside one of the other spheres. In the SCF procedure, the surface-point charges are determined from the charge density and corresponding potential of the molecule itself, and the electrostatic equations assuming, for the moment, a perfect conductor solvent, i.e., a vanishing potential on the cavity surface. This particular assumption makes

the equations a lot easier and faster to solve. The actual dielectric value of the medium defines a correction factor for computed properties such as the energy.

FIRST-ENERGY DERIVATIVES

Geometry Optimization

The (first) derivatives of the energy with respect to nuclear displacements are calculated analytically for a particular geometry at the end of the SCF procedure.[74, 144, 145] They are used to identify stationary points in the energy surface, notably for the automatic optimization of the molecular structure. This is carried out by a Newton-type iterative procedure, based on a quadratic local approximation of the energy surface and an initial estimate of the Hessian—based on a force-field approximation incorporated in the program or read-in from a restart file, for instance, obtained from an explicit ADF calculation of harmonic frequencies.[75, 146] At each step in the optimization the estimate of the true Hessian is improved by an updating procedure using the difference of current and previous gradients in relation to the difference in geometries. Various Hessian update schemes are available in ADF. The default (for normal geometry optimization) is the BFGS (Broyden Fletcher Goldfarb Shanno) method,[147] which contains a bias to keep the Hessian positive-definite, which should be the case near an energy minimum.

Transition States[148]

Transition states are of high chemical interest but computationally often hard to pinpoint. Moreover, the accuracy of the results may be very critical when, for instance, the energy barrier between reactants and products is required at kcal precision. At first sight, the determination of a transition state (TS) is very similar to a minimization. A stationary point is searched where the gradient vector vanishes. The Hessian is updated in an iterative procedure, after some kind of initial estimate. The difference between a TS search and a minimization is only that at the TS the Hessian has a negative eigenvalue.

When we are close enough to the TS, the standard procedure used for minimization will produce the TS. However, the energy surface around the TS often displays sizeable anharmonicity. Neglecting third- and higher-order terms, as inherent to the Newton approach, is therefore likely to be less accurate. Moreover, taking wrong or too large steps in a minimization usually keeps us in the local "bowl" containing the minimum so that the gradients at any new geometry still point more or less towards the minimum. With transition states, however, it is much more common that a too-large step brings us to a location where the energy surface has little resemblance anymore to the surface close to the TS, and the procedure easily loses sight completely of where the TS might be. The aspects that discriminate TS search implementations from a simple minimization are largely related to these considerations. In the first place, a different Hessian update scheme is applied: obviously we have no reason to apply a method that favors a positive definite Hessian. Second, control by the program of, for instance, a maximum step length to take at each optimization step is tighter. Third, checks are performed to verify that the Hessian has the right structure (one negative eigenvalue) and, if it is found otherwise, adjustments are applied, all this to avoid that the procedure wanders away from the TS and loses track.[148] Despite such precautions, a successful search for a TS often requires that the initial Hessian is fairly accurate. A force field-based estimate may then be inadequate, and one has to perform a calculation of frequencies first and feed the result into the TS run, which makes the whole procedure more cumbersome and time-consuming.

A reasonable first estimate of the TS, crucial for the successful application of the TS search algorithm, can, in many cases, be identified by a linear transit procedure as described in the next section.

Reaction Path by a Linear Transit

One of the options in ADF is to scan a path on the energy surface. The path is defined by a systematic variation of one or more nuclear coordinates between user-specified initial and final values. The coordinates that are so varied are denoted the linear transit (LT) parameters. If there is more than one such parameter, all of them are varied simultaneously; the linear transit is therefore often called a *synchronous* linear transit. For each LT point on the scan, defined by a particular value of the path parameter(s), the remaining nuclear coordinates (or a subset of them), i.e., those that are not LT parameters, may be optimized. From a technical point of view, a LT run is simply a sequence of constrained optimizations.

One of the most useful applications of a LT is to get a reasonable estimate of a transition state. A classical example is the HCN to CNH transit, in which the hydrogen atom travels from one end of CN to

the other. The LT parameter would here be the angle θ(H–C–N), changing from 180 degrees down to zero in 10 steps, say. For each particular θ-value, the HC and CN distances are optimized. By gathering the energy values at the LT points and interpolating them in a curve we obtain a fair view of the path, and hence, the location of the TS.

Intrinsic Reaction Coordinate (IRC)

For insight in the properties of a full reaction path the LT functionality provides only very crude information. An alternative and more advanced procedure to trace the path of a chemical reaction is provided by the intrinsic reaction coordinate (IRC) method[149] as implemented in ADF.[76, 150] The basic idea[151] is to start at a transition state and "slide" down the hill towards the adjacent local minimum, at either side of the transition state, by following the line of steepest decent in the metric of mass-weighted coordinates. A full determination of the path does not only produce the height of the barrier in a reaction, but also provides information for thermodynamic properties, the reaction rate and dynamics;[152] the details of such analysis have not yet been implemented in ADF.

The calculation starts by taking steps of controlled length (in the mass-weighted metric) towards the minimum by determining the minimum on the local "sphere" around a given point along the path, with as radius the chosen step length. The calculation, therefore, consists, as in the linear transit method, of a sequence of constrained optimizations, and terminates when the adjacent minima to the TS have been identified.

SECOND DERIVATIVES: FREQUENCIES AND IR SPECTRA

Frequencies

The original (and still available) implementation of harmonic frequencies in ADF[75, 153] computes second derivatives of the energy with respect to nuclear displacements by numerical differentiation of the analytically computed *first* derivatives (gradients) in the geometry at hand and a series of slightly modified geometries. Going over all possible displacements, we obtain the matrix of force constants, which we can express in mass-weighted Cartesian coordinates q_i.

$$F_{ij} = \frac{\partial^2 E}{\partial q_i \partial q_j} \qquad (26)$$

$$q_i = x^{(1)}\sqrt{m^{(1)}}, \qquad q_2 = y^{(1)}\sqrt{m^{(1)}},$$
$$q_3 = z^{(1)}\sqrt{m^{(1)}}, \qquad q_4 = x^{(2)}\sqrt{m^{(2)}}, \qquad \ldots \qquad (27)$$

Diagonalization of F, after projecting out the rigid translations and rotations, gives the normal modes as eigenvectors. The eigenvalues are directly related to the harmonic frequencies.

$$v_k = \frac{\sqrt{\lambda_k}}{2\pi} \qquad (28)$$

When building the matrix of force constants, one can use Cartesian or internal (Z-matrix) displacements. In both cases the final matrix is transformed to the representation in mass-weighted Cartesians and then diagonalized to obtain the frequencies and normal modes.

It is possible to run a calculation of frequencies where only a subset of the nuclear coordinates is displaced, thereby neglecting any coupling with the other coordinates. This is a fast way to study a few well-selected normal modes if one knows *a priori* that the omitted displacements will hardly contribute to the mode(s) one is interested in.

In the computation of second energy derivatives by numerical differentiation of first derivatives in slightly differing geometries, accuracy of the gradients is crucial. This puts high demands on numerical integration precision, SCF convergence, etc. Furthermore, for each of the displaced geometries a full SCF has to be carried out to determine the gradients. This makes the computation of frequencies by numerical differentiation a demanding task, although in the ADF program use is made of symmetry[148, 153] so that only symmetry unique atoms are displaced.

There are indications that ADF frequencies are slightly superior to frequencies computed with programs that use Gaussian-type basis of comparable size.[154]

Analytical Second Derivatives

Use of *analytical* second derivatives avoids the numerical differentiation of gradients, which is rather critical for precision of the results, *and* it removes the necessity to perform many SCF cycles. At the other hand, one needs to solve the coupled perturbed Kohn–Sham equations where both derivatives are taken with respect to the nuclear coordinates.[155, 156] Analytical second derivatives are faster *and* more robust and accurate, and have recently become available (in the export version of the package) as a separate program that takes the normal (TAPE21) result file from an ADF calculation as input.

Infrared (IR) Intensities[75, 153]

As a by-product in the calculation of second energy derivatives—harmonic frequencies—one obtains the first derivatives of the dipole moments, yielding the infrared (IR) intensities.

$$A_i = (974.86)g_i \left(\frac{\partial \mu}{\partial Q_i} \right)^2 \qquad (29)$$

Q_i is the normal mode (mass-weighted Cartesians in atomic units, masses in atomic mass units) with degeneracy g_i; A_i is the absorption intensity in [km/mol] of normal mode Q_i, and μ is the dipole moment in atomic units. IR intensities are obtained both with the analytic and with the numeric approach to second derivatives.

Raman intensities are calculated similarly from the derivatives of the polarisability tensor with respect to the normal modes (see also TDDFT section).

ELECTROMAGNETIC PROPERTIES

NMR Chemical Shifts

The ADF package allows the calculation of the shielding tensor of nuclear magnetic resonance (NMR) spectroscopy.[77, 78, 80–82, 157] A separate NMR module that reads information about the molecule from the standard TAPE21 output file of an ADF run calculates the shielding data. The method has been formulated in the framework of gauge including atomic orbitals (GIAO) and includes relativistic effects (ZORA or Pauli, scalar or including spin-orbit effects).

The calculation of NMR parameters constitutes a theoretically challenging task, in particular when applied to heavy elements. An earlier investigation suggested that the frozen core approximation—attractive because of its efficiency and necessary for relativistic calculations with the Pauli formalism—would not be appropriate for shielding calculations. However, when terms that contain the core orthogonalization coefficients to first order in the magnetic field are taken into account, as in the ADF implementation, the differences between frozen core and all-electron calculations are found to be small. One has to take care, however, that the valence includes at least the highest atomic shells *and* the next to highest (*p*- and *d*-shells).

The NMR shielding tensor is the second derivative of the energy with respect to the magnetic field B_k in each direction $k = x, y, z$, and the magnetic moment of the nucleus μ_t in each direction $t = x, y, z$

$$\sigma_{kt} = \frac{\partial^2 E}{\partial B_k \partial \mu_t} \qquad (30)$$

This symmetric 3×3 tensor relates the magnetic field that is externally applied in the NMR experiment, $\mathbf{B}^{\text{ext}}$, to the effective magnetic field that is felt at the nucleus, $\mathbf{B}^{\text{eff}}$

$$\mathbf{B}^{\text{eff}} = \sigma \mathbf{B}^{\text{ext}} \qquad (31)$$

The isotropic shielding is the average of the diagonal elements of the tensor. The difference in isotropic shielding of a reference material and the sample gives the NMR shift of a standard NMR experiment. The program calculates the absolute shielding, as it has no knowledge of reference materials.

In the full equation for the tensor, we can discriminate three terms: the paramagnetic and diamagnetic contributions, and a spin contribution. The latter is the Fermi-contact term if the Pauli spin-orbit Hamiltonian is used, or the spin-orbit coupling contribution in the ZORA approach. The three contributions to the tensor are calculated separately (the spin-orbit term only in a spin-orbit calculation). The GIAO formalism makes it possible to analyze the contributions to the shielding in terms of orbital contributions.[158–163]

NMR Spin-Spin Coupling

Implementations are under way of methods that will calculate NMR spin–spin coupling constants.[164–167]

ESR

ADF supports the computation of Electron Spin Resonance (ESR) properties in systems with one unpaired electron: the g-tensor, A-tensor (nuclear magnetic dipole Hyperfine interaction), and Q-tensor (nuclear electric quadrupole hyperfine interaction).[168–172] Work on ESR calculations for systems with more than one unpaired electron is in progress.

TIME-DEPENDENT DFT

Time-dependent DFT (TD-DFT)[173] has been implemented in ADF[174, 175] for the research of response properties, such as excitation energies, frequency-dependent (hyper)polarizabilities and related properties of (at the moment) closed-shell molecules. The implementation exploits the molecular symmetry and typically requires similar amounts of CPU time as an ordinary SCF calculation in ADF.

The time-dependent Kohn–Sham equations are similar to the time-independent ones

$$i\frac{\partial}{\partial t}\varphi_i(\mathbf{r}, t) = H\varphi_i(\mathbf{r}, t) = \left(-\frac{\nabla^2}{2} + V[\rho](\mathbf{r}, t)\right)\varphi_i(\mathbf{r}, t)$$
(32)

$$\rho(\mathbf{r}, t) = \sum_j n_j |\varphi_j(\mathbf{r}, t)|^2$$
(33)

The potential V comprises the Coulomb potential due to the electron cloud, the nuclear and any other external potentials, and an effective exchange–correlation (XC) potential, all of them time-dependent. In principle, the effective potential is different from the one defined in the KS formulation of ground-state DFT. However, it is a good approximation (the adiabatic approximation) in many cases to assume that the functional dependence of the time-dependent effective potential on the time-dependent density is the same as the dependence of the time-independent potential on the time-independent density.

The objective is to determine the response of the system—the change in the density—to a change in the external field. Using a perturbative approach, the density is expanded in a functional Taylor series (in the perturbing potential). Many interesting properties, for instance, the polarizability and excitation energies, depend only on the first-order cnange in the density.

The first-order density depends on the (exact) linear response function χ. After a Fourier transformation we can rewrite the time-dependent equations in frequency (energy)-dependent form

$$\delta\rho_1(\mathbf{r}, \omega) = \int d\mathbf{r}' \, \chi(\mathbf{r}, \mathbf{r}', \omega)\delta V_{\text{ext}}(\mathbf{r}', \omega)$$
(34)

In the Kohn–Sham formulation of time-dependent DFT the response function is replaced by the response function χ_s of the noninteracting Kohn–Sham system, while the external potential is replaced by the effective Kohn–Sham potential. The response function χ_s can be expressed in the *unperturbed* KS orbitals

$$\chi_s(\mathbf{r}, \mathbf{r}', \omega) = \sum_{jk}(n_k - n_j)\frac{\varphi_j(\mathbf{r})\varphi_k^*(\mathbf{r})\varphi_j^*(\mathbf{r}')\varphi_k(\mathbf{r}')}{\omega - (\varepsilon_j - \varepsilon_k) + i\eta}$$
(35)

If we consider the real density response in an applied electric field, we can choose the complex KS orbitals to be real-valued and the infinitesimal η can be set to zero. Assuming, furthermore, that the occupation numbers n_j are all either 1 or zero, the

equation becomes

$$\chi_s(\mathbf{r}, \mathbf{r}', \omega) = \sum_i^{\text{occ}} \sum_a^{\text{virt}} \varphi_a(\mathbf{r})\varphi_i(\mathbf{r})\varphi_a(\mathbf{r}')\varphi_i(\mathbf{r}')$$
$$\times \left(\frac{2(\varepsilon_i - \varepsilon_a)}{(\varepsilon_i - \varepsilon_a)^2 + \omega^2}\right)$$
(36)

(Note: if we replace $+\omega^2$ by $-\omega^2$, we obtain the polarizabilities at imaginary frequencies, which are used for the determination of Van der Waals dispersion coefficients.)

In the TDDFT case, one has to consider the response of the noninteracting KS system (described by the single-particle KS response function) to an *effective* field, schematically written as:

$$\delta\rho = \chi_s \delta V_{\text{eff}}$$
(37)

The change in the effective potential δV_{eff} in eq. (37) is split in its Coulomb, external, and XC components.

$$\delta V_{\text{eff}} = \int d\mathbf{r}' \frac{\delta\rho(\mathbf{r}', \omega)}{|\mathbf{r} - \mathbf{r}'|} + \delta V_{\text{ext}}(\mathbf{r}, \omega) + \delta V_{\text{XC}}(\mathbf{r}, \omega)$$
(38)

The latter is related to the so-called XC kernel f_{XC}, which is the functional derivative of the time-dependent XC potential with respect to the time-dependent density.

$$\delta V_{\text{XC}}(\mathbf{r}, \omega) = \int d\mathbf{r}' f_{\text{XC}}(\mathbf{r}, \mathbf{r}'; \omega)\delta\rho(\mathbf{r}', \omega)$$
(39)

$$f_{\text{XC}} = \frac{d^2}{d\rho^2}\left(\rho\varepsilon_{\text{XC}}[\rho]\right)_{\rho = \rho_0}$$
(40)

Here ε_{XC} is the XC energy functional.

In ADF, the adiabatic (local density) approximation (ALDA) is used for the kernel. Although this kernel, which is then the functional derivative of the ordinary LDA XC potential, is local in both space and time, it has performed quite well in practical calculations. There are strong indications[128, 129, 176] that the approximation chosen for the usual XC potential in the SCF part of the calculation has much more impact on the accuracy of calculated response properties.

Equations (37)–(40) are solved self-consistently in an iterative fashion, using the external potential as initial guess for the effective potential; in other words, in the first iteration one neglects all XC and Coulomb screening effects. Rapid convergence is obtained if DIIS techniques are used in the iterative update procedure, similar as for the ordinary SCF cycles in ADF.

Linear Response Properties

The linear response of a molecule to a frequency dependent electric perturbation is given by the linear polarizability tensor $\alpha_{ij}(\omega)$.

$$\mu_i = \mu_i^0 + \sum_j \alpha_{ij}(\omega)E_j(\omega) \qquad (41)$$

$(\mu_i - \mu_i^0)$ is the change in the dipole moment of the molecule in direction i. Having solved the SCF equations for the first-order change in the density, we obtain the polarizability by

$$\alpha_{ij}(\omega) = -\frac{2}{E} \int d\mathbf{r}\, \delta\rho_i(\mathbf{r}, \omega)\mathbf{r}_j \qquad (42)$$

The poles of the polarizability tensor are the (vertical) excitation energies, while the strengths of these poles are given by the oscillator strengths. The relation between the oscillator strengths, excitation energies, and average dipole polarizabilities is given by:

$$\alpha_{av}(\omega) = \sum_i \frac{f_i}{\omega_i^2 - \omega^2} \qquad (43)$$

The polarizability also leads directly to the (isotropic) Van der Waals dispersion coefficient C_6 that determines the long-range dipole–dipole dispersion interaction between two systems, A and B. (This applies to atoms; molecules have also an anisotropic contribution to the R-6 interaction.)

$$E_{\text{disp}} = \frac{C_6(A, B)}{R_{AB}^6} \qquad (44)$$

$$C_6(A, B) = \frac{3}{\pi} \int_0^\infty \alpha_A(i\omega)\alpha_B(i\omega)\, d\omega \qquad (45)$$

The isotropic polarizability α is the average of the diagonal elements of the tensor.

Instead of a perturbative dipole field $E\hat{\mathbf{r}}\cos(\omega \mathbf{t})$, we may apply a more general multipole electric field. This yields the general multipole–multipole polarizability $\alpha_{mm'}$, which describes the response of a general molecular multipole moment q^{lm} to such a field.

$$q^{lm} = q_0^{lm} + \sum_{l'm'} \alpha_{mm'}E^{l'm'} \qquad (46)$$

The $l = 2$ (quadrupole) and $l = 3$ (octupole) cases have been implemented in ADF.[177] In fact, one can obtain all components $\alpha_{mm'}$ up to $l = 3$ for a range of frequencies in a single calculation. Similar to the isotropic dispersion coefficients of eq. (45), one can obtain all isotropic and anisotropic dispersion coefficients between two molecules from a calculation that uses the result files of response calculations on the separate monomers.[177]

Excitation Energies and Oscillator Strengths

TDDFT offers a rigorous theoretical framework for the calculation of excitation energies in DFT, and is preferable in this respect to ΔSCF approaches to reach the same goal.[175, 178, 179] The basic equation for the determination of excitation energies and oscillator strengths is the following eigenvalue equation

$$\Omega F_i = \omega_i^2 F_i \qquad (47)$$

The linear dimension of the matrix Ω is the product of the numbers of virtual and occupied orbitals, respectively. Because of its large size, this matrix cannot be diagonalized directly. Instead, the iterative Davidson procedure is invoked to obtain a few of the lowest excitation energies and oscillator strengths of each irrep. The matrix Ω contains the same Coulomb and XC terms as are needed for the calculation of the polarizability tensor. In fact, the average dipole polarizability and its frequency dependence (determined by the so-called Cauchy coefficients) can also be determined if a direct diagonalization of the matrix is possible.

The Ω matrix is blocked by symmetry, and can be split in singlet and triplet parts, each of which is handled in turn in the implementation. Oscillator strengths, which determine the magnitudes of the peaks in an absorption spectrum, are calculated from the solution vectors F_i. An example of a chemical application of this part of the code is given in the second part of this article.

Nonlinear Response

Higher order optical response is governed by the hyperpolarizability tensors β, γ, etc.

$$\mu_i = \mu_i^0 + \sum_j \alpha_{ij}E_0^j + \frac{1}{2!}\sum_{jk}\beta_{ijk}E_0^j E_0^k$$
$$+ \frac{1}{3!}\sum_{jkl}\gamma_{ijkl}E_0^j E_0^k E_0^l + \cdots \qquad (48)$$

β is the first hyperpolarizability tensor (which vanishes for molecules with an inversion center), γ is the second hyperpolarizability tensor, etc. If the external field is static, these tensors can be calculated with finite field techniques. In the experiment one always measures frequency-dependent hyperpolarizabilities. For a direct comparison to experiment it is, therefore, important to include this frequency dependence as implemented in ADF.[180]

Derivatives w.r.t. Nuclear Coordinates

The variation of spectroscopic properties upon nuclear displacement gives access to several properties. To compute this geometric dependency for small displacements we need the geometric derivatives at the equilibrium geometry. These are obtained as in a normal calculation of harmonic frequencies, namely by numerical differentiation, using the data at the equilibrium geometry and at slightly displaced geometries (some of the applications have yet to be implemented). Derivatives of the dipole moment give rise to the IR intensities. The derivatives of the polarizability tensor α likewise yield the intensity and depolarization ratio of Raman scattering (as a function of the laser frequency in our case). Derivatives of the hyperpolarizability tensors govern the hyper-Raman effect, while derivatives of the excitation energies can be used to estimate the intensity of the resonance Raman effect. So far, only the IR and Raman intensities have been implemented in ADF.

Geometrical derivatives are not only interesting because they give rise to additional properties, but they also determine the vibrational average of a quantity, which is usually what is measured experimentally.

Combination with Relativistic Options

All functionality of the RESPONSE module can be combined with the scalar relativistic options of ADF, such as the scalar Pauli and scalar ZORA options. It is not yet possible to include spin-orbit effects on response properties. If scalar relativistic effects are taken into account, the relativistic orbital energies and orbitals are used in the post-SCF excitation energy or polarizability calculation. No further relativistic effects are included in the calculation of the density response. By default the so-called "scaled" ZORA orbital energies are used (see ref. 181 for a discussion and an application).

Part II. Applications: The Chemical Bond

The scope of applicability of modern DFT codes is rapidly expanding as a result of extended functionality and increased efficiency of the implementations, reaching such diverse fields as organic, organometallic, and inorganic chemistry and even biochemistry, covering the gas phase as well as the
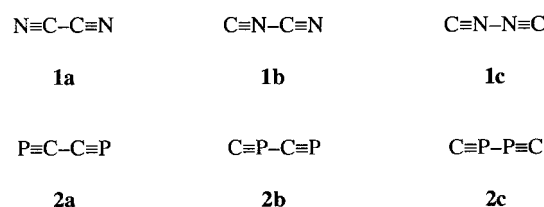
$N{\equiv}C{-}C{\equiv}N$	$C{\equiv}N{-}C{\equiv}N$	$C{\equiv}N{-}N{\equiv}C$
1a	**1b**	**1c**
$P{\equiv}C{-}C{\equiv}P$	$C{\equiv}P{-}C{\equiv}P$	$C{\equiv}P{-}P{\equiv}C$
2a	**2b**	**2c**

FIGURE 6. Lewis structures of linear CN (**1**) and CP (**2**) dimers.

solid state and chemistry in solution. In the remainder of this article, we elaborate first on two of chemistry's core issues: the chemical bond (this section) and chemical reactions (next section). Thereafter, an application in the field of biochemistry is briefly discussed, namely, the structure and bonding of deoxyribonucleic acid, DNA. The emphasis is on gaining insight, on being able to tell how a certain overall effect is brought about by the underlying electronic mechanisms. More than once this reveals surprising differences between seemingly similar phenomena, and vice versa. This is of great practical importance. Not only does it yield a deeper understanding of the investigated molecule, but it also allows a more rational tuning of the system to achieve the desired properties.

In this chapter, we look into the elementary concepts of the electron-pair bond, the three-electron bond, and the donor–acceptor (or charge transfer) bond in various chemical situations, and we evaluate these concepts within the framework of the quantitative Kohn–Sham MO model. These bonding modes may interfere with and can be substantially affected by Pauli repulsion with closed shells (or same-spin electrons in open shells) and by classical electrostatic interactions.

THE ELECTRON-PAIR BOND

An interesting example of similar trends that originate from very different electronic mechanisms is provided by the two valence iso-electronic series of CN and CP dimers,[182, 183] schematically shown in Figure 6, series **1a–c** and **2a–c**, respectively.

We have studied these systems at the BP86/TZ2P level. All three CN dimers have linear equilibrium structures and it is only the most stable CP dimer, PCCP (**2a**) that acquires such an unbent geometry. In fact, CPCP and CPPC actually tend toward nonlinear geometries, the linear structures **2b** and **2c** being second- and fourth-order saddle points. This has been investigated and analyzed in detail.[183] In the following, we focus on the linear species, and

in particular, on the central electron-pair bond that holds together the monomers in **1** and **2**.

The strength of the central bond decreases in both series of CX (X = N, P) dimers if we go from coupling via carbon to coupling via the heteroatom. The bond dissociation enthalpies (BDE) for 298 K are 136.6, 113.5, and 68.2 kcal/mol along **1a–c**, and 152.2, 68.7, and 7.5 kcal/mol along **2a–c**. In the CN dimers, the decrease in bond strength goes with a *shortening* of the bond (1.373, 1.305, and 1.274 Å along **1a–c**), whereas in the CP dimers it is accompanied by bond *elongation* (1.336, 1.709, and 2.216 Å along **2a–c**). The relatively short C—C bond distance in **1a** and **2a** is indicative of a partial multiple-bond character, which is confirmed by our analysis. Thus, the as-yet unisolated PCCP (**2a**) is thermodynamically stable. However, as follows from further explorations, **2a** may tend to polymerise. Synthetic strategies toward this molecule have to cope with this instability, for example, through coordination of the product to transition metals.[183] The analysis, furthermore, shows that the contraction along **1a–c** is due to the combined effect of the smaller effective size of nitrogen compared with carbon, and to its higher electronegativity. The singly occupied molecular orbital (SOMO) of CN, which is weakly antibonding, has a lower amplitude on nitrogen. These effects lead to an onset of both repulsive and bonding interactions at shorter bond length if N instead of C is involved in the central bond. The fact that the central bond along **2a–c** nevertheless *elongates* when CP binds via P instead of C is simply due to the more diffuse character and larger effective size of phosphorus compared to carbon or nitrogen.

We may wonder what cause underlies the similar trends of decreasing BDE for the CN and CP dimer sequences **1** and **2**. The relevant frontier orbitals of the CX monomers, i.e., the σ_{HOMO} and σ_{SOMO} in σ symmetry schematically represented in Figure 7 (for contour plots, see ref. 183), are essentially C—X nonbonding orbitals.

The former provides the axial N or P lone pair, whereas the latter carries the unpaired electron. An important feature of the CN and CP frontier orbitals is their delocalized nature, with significant
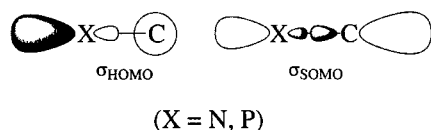
$(X = N, P)$

FIGURE 7. Frontier orbitals of CX⁺ radicals, X = C, P.

FIGURE 8. The CN and CP dimers can be considered ambident radicals.

amplitude at both ends of the diatomic. The σ_{HOMO} has somewhat more amplitude on the heteroatom (it is the N or P lone pair orbital), whereas the σ_{SOMO} has a slight bias toward the carbon atom. In other words, CN and CP are ambident radicals (see Fig. 8) that may, in principle, form electron-pair bonds (Fig. 9) either via carbon or via the heteroatom, leading to **1a–c** and **2a–c**.

As the σ_{SOMO} has a bigger lobe on carbon, one may expect that the strength of the electron-pair bond (Fig. 9) and the stability of the dimer decreases in the order XC—CX > CX—CX > CX—XC (X = N, P).

At first sight this is nicely confirmed by the decreasing bond strengths along the series **1a–c** and **2a–c** (Fig. 8). However, a more quantitative analysis shows that, below the surface of the overall bond strength, these similar trends have quite different origins. In the CN dimers, the reduction in bond strength is caused by an enormous increase in the ΔE^0 repulsion (see the Bonding Energy Analysis section) from 144.3 to 371.3 kcal/mol, which is not fully compensated by a sizeable increase in ΔE_{oi} from −288.2 to −446.5 kcal/mol. In contrast, in the CP dimers, the bond strength decreases because of a weakening of the bonding orbital interactions ΔE_{oi} (from −320.9 to −104.1 kcal/mol), especially those associated with the σ bond (ΔE_σ) despite an opposite trend of the repulsion ΔE^0, which actually decreases (from 161.5 to 91.0 kcal/mol).

The increase in Pauli-repulsion along the CN dimers **1a–c** is easy to understand. It is caused by the increase in overlap between the closed-shell σ_{HOMO} orbitals (Fig. 7) and between the π_{HOMO} orbitals (not shown), which have higher amplitudes on nitro-
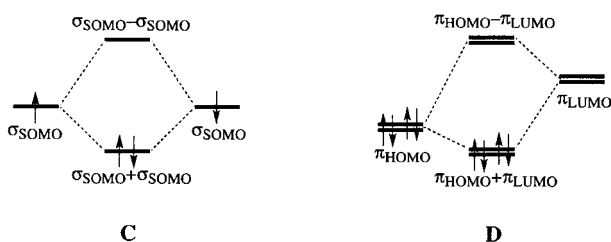
FIGURE 9. σ electron-pair (left) and π donor–acceptor (right) orbital interaction diagram for CN (**1**) and CP (**2**) dimers.

gen. The increase in stabilizing orbital interactions along **1a–c**, however, does not correlate with the bond overlap $\langle \sigma_{SOMO} | \sigma_{SOMO} \rangle$ that, as qualitatively predicted, *decreases* from 0.46 to 0.21. Here we see a subtle interplay of "secondary" $\sigma_{SOMO} \pm \sigma_{HOMO}$ interactions that interfere with the pure electron-pair bond. To first order, the primary $\sigma_{SOMO} + \sigma_{SOMO}$ interaction decreases in strength along **1a–c** (Fig. 6) and the $\sigma_{SOMO} + \sigma_{SOMO}$ in NCCN (**1a**) descends strongly, and comes out close to (in fact, even below) the $\sigma_{HOMO} + \sigma_{HOMO}$. This gives a strong mutual repulsion and a corresponding weakening of the electron pair bonding interaction contained in ΔE_{oi}. In contrast, in CNNC (**1c**) the occupied $\sigma_{HOMO} - \sigma_{HOMO}$ is strongly destabilized, due to a sizeable overlap and repulsion between the N lone pair orbitals, and it approaches in first order the unoccupied $\sigma_{SOMO} - \sigma_{SOMO}$ from below. The resulting donor–acceptor interaction is about twice as strong as that in **1a** and ΔE_{oi} in **1c** is, hence, significantly more bonding.[182] Without this secondary interference of the pure electron-pair bond with other closed shell orbitals the differences in bond strength along **1a–c** would have been much larger, i.e., NCCN would have been more and CNNC less stable.

It remains to understand why the repulsive and bonding orbital interactions in the three linear CP dimers follow the opposite trend with respect to those in the CN dimers, i.e., why both ΔE^0 and ΔE_{oi} *decrease* along **2a–c**. In the first place, the CP orbitals are more extended and diffuse at the P side. So, the overlaps are smaller and achieve a lower maximum at a longer bond distance when phosphorus gets involved in the central bond. Consequently, the Pauli-repulsion contained in ΔE^0 and, even more so, the bonding orbital interactions ΔE_{oi} *decrease* along **2a–c** instead of increasing as they do along **1a–c**. The other important point is that the primary or "first-order" electron pair bond is much less affected by secondary interactions with other orbitals: the decrease in $\sigma_{SOMO} + \sigma_{SOMO}$ electron-pair bonding, if we go from **2a** to **2c**, is no longer compensated by a strongly stabilizing $\sigma_{HOMO} / \sigma_{SOMO}$ interaction. This is simply due to the fact that the $\sigma_{HOMO} - \sigma_{HOMO}$ does no longer come close enough to the empty $\sigma_{SOMO} - \sigma_{SOMO}$ because of the smaller $\sigma_{HOMO} \pm \sigma_{HOMO}$ splitting in the CP dimer, and because of the larger $\sigma_{HOMO} / \sigma_{SOMO}$ gap in the CP monomer (3.5 eV in CP compared to 2.4 eV in CN).

Finally, a decomposition of the bonding orbital interactions shows a smaller but significant contribution of donor–acceptor-type π-bonding between a (doubly degenerate) set of occupied π_{HOMO} orbitals on one CX monomer (X = N, P) and the
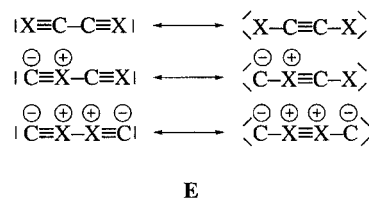

FIGURE 10. Simple VB resonance schemes for linear CN (**1**) and CP (**2**) dimers.

corresponding set of unoccupied π^*_{LUMO}s on the other CX monomer (Fig. 9**D**). In CNNC (**1c**), the π orbital interactions (-85.8 kcal/mol) are even larger than the net bond enthalpy of -68.2 kcal/mol (the σ orbital interactions in **1c** are -360.7 kcal/mol). Therefore, the central bond in the CX dimers is best conceived as having partial triple bond character, as shown in *E* in terms of a resonance between simple VB structures (Fig. 10).

THE THREE-ELECTRON BOND AND ITS ONE-ELECTRON BONDING COMPONENT

The traditional picture in MO theory of the two-center three-electron (2c–3e) bond between a closed-shell and a radical fragment, A and B say, is that of a doubly occupied bonding MO (σ) and a singly occupied antibonding MO (σ^*) of the composite molecule A∴B (Fig. 11).

It follows from Figure 11 that the 2c–3e bond may be viewed as composed of an electron-pair bond counteracted by a destabilizing antibonding electron leading formally to a bond order of 1/2. The above analysis considers the overall molecule and the properties of its MOs.

Recently, we have proposed a different—although equivalent—approach to the 2c–3e bond, namely from the perspective of the fragments and their mutual interaction.[184] We take the sulphur–sulphur three-electron bond in $H_2S∴SH_2^+$ as an example ($H_2S∴SH_2^+$ is the only minimum on the MP2/6-31G* potential energy surface of $H_4S_2^{+\cdot}$ [185, 186]). This species is the archetype of
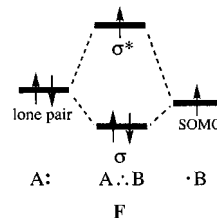

FIGURE 11. The two-center three-electron (2c–3e) bond.

dialkylsulfide dimer radical cations ($R_2S \cdot SR_2^+$), a class of systems for which there is also much interest in gas-phase experimental studies.[187–190]

At the BP86/TZ2P level we find the $H_2S \cdot SH_2^+$ system bound by a sulphur–sulphur bond of 2.886 Å with a bond enthalpy for 298 K of -40.7 kcal/mol. This bond enthalpy is some 10 kcal/mol stronger than the best *ab initio* estimate [-31.9 kcal/mol at CCSD(T)]. This relatively large error for the nonlocal functionals can be attributed to a well-known deficiency of the existing exchange functionals to properly cancel the self-interaction part of the Coulomb energy in case of delocalized ionization out of symmetry equivalent weakly (or non-) overlapping orbitals.[191, 192] To asses if this deficiency of the functionals might affect the physical model of the 2e–3e bond, we have carried out the quantitative analysis at various levels of DFT, local ($X\alpha$-VWN) as well as nonlocal (BP86 and PW91). It appears that, although numerically different, the relative proportions of the different physical terms (ΔV_{elst}, ΔE_{Pauli}, ΔE_{oi}) in the S–S interaction are very similar for all three levels, yielding the same physical picture. The subsequent discussion is based on the BP86/TZ2P calculations, which give the least overbinding.

The sulphur–sulphur bond in $H_2S \cdot SH_2^+$ is mainly provided by the three-electron orbital interactions between the $1b_1$ orbitals of the two fragments, i.e., the $3p_x$ lone-pair of H_2S and the $3p_x$ SOMO of $H_2S^{+\bullet}$ (e.g., Fig. 11). Combining the repulsive and bonding orbital interactions into one term, $\Delta E_{2c-3e} = \Delta E_{Pauli} + \Delta E_{oi}$, one arives at a three-electron interaction ΔE_{2c-3e} of -25.9 kcal/mol. This is about 60% of the net interaction ΔE_{int}. However, the electrostatic interaction ΔV_{elst} although clearly smaller than ΔE_{2c-3e}, is an important component also: with -18.4 kcal/mol it still contributes somewhat more than 40% to the net sulphur–sulphur interaction ($\Delta E_{int} = -44.3$ kcal/mol).

Figure 12 illustrates how the three-electron bond (**G**) can be interpreted in the fragment approach. The repulsive term ΔE_{Pauli} contained in ΔE_{2c-3e} is mainly due to the destabilizing interaction **H** between the unpaired $3p_x\alpha$ electron on $H_2S^{+\bullet}$ and the same-spin $3p_x\alpha$ electron of the lone-pair on H_2S (the excess spin is arbitrarily chosen α). The bonding orbital interaction ΔE_{oi} is simply provided by a one-electron bond **I** between the $3p_x\beta$ electron of the lone-pair on H_2S and the empty $3p_x\beta$ orbital on $H_2S^{+\bullet}$, i.e., $\Delta E_{oi} \simeq \Delta E_{2c-1e}$. In this way, the three-electron bond is naturally linked to the one-electron bond plus a characteristic Pauli repulsive term. Important also is that we are able to quantify the different energy terms in the overall
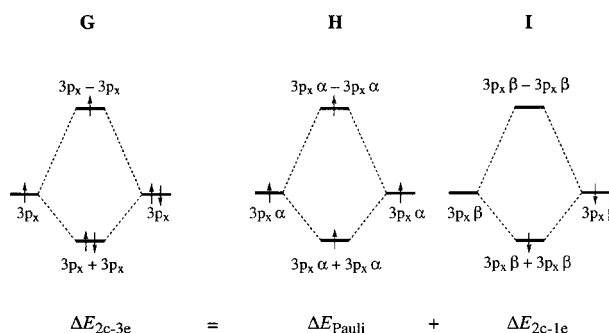

FIGURE 12. Decomposition of the two-center three-electron bond.

bond energy. This places the physical model on a more quantitative basis. In particular, it becomes clear that the three-electron bond is, in principle, weaker than the corresponding one-electron bonding component. In our $H_2S \cdot SH_2^+$ model system, for example, the three-electron bond ($\Delta E_{2c-3e} = -25.9$ kcal/mol) is about twice as weak as the corresponding one-electron bonding component ($\Delta E_{2c-1e} = \Delta E_{oi} = -51.3$ kcal/mol) owing to the Pauli repulsive term ($\Delta E_{Pauli} = 25.4$ kcal/mol).

THE ROLE OF PAULI STERIC REPULSION IN BONDING MODELS

So far, we have looked at different modes of *bonding* and how Pauli-repulsive orbital interactions may either influence them (e.g., the electron-pair bond) or be an essential part (2c–3e bond). In this section, we examine a different role of Pauli repulsion, namely its role as the source of steric repulsion between nonbonded groups. An interesting example is the methyl radical and its heavier Group-14 congeners, $AH_3^{\bullet}$ (A = C, Si, Ge, Sn). The methyl radical is known to be planar (D_{3h}), whereas the heavier $AH_3^{\bullet}$ radicals adopt pyramidal (C_{3v}) structures. This is nicely confirmed in a recent BP86/TZ2P study,[193] which shows that the H—A—H angle β in $AH_3^{\bullet}$ decreases ($\beta = 120, 112.7, 112.4$, and $110.6°$), whereas the inversion barrier increases along A = C, Si, Ge, and Sn (0.0, 3.7, 3.8, and 7.0 kcal/mol).

On the basis of the qualitative MO theory, this was traditionally explained through the operation of a second-order Jahn–Teller effect (Fig. 13).[194, 195] The mixing between the nonbonding np_z SOMO and the A—H antibonding LUMO stabilizes and pyramidalizes $AH_3^{\bullet}$. This effect is more pronounced for the heavier (more electropositive and diffuse) central atoms A. The SOMO–LUMO gap becomes smaller due to the higher energy of the np_z SOMO
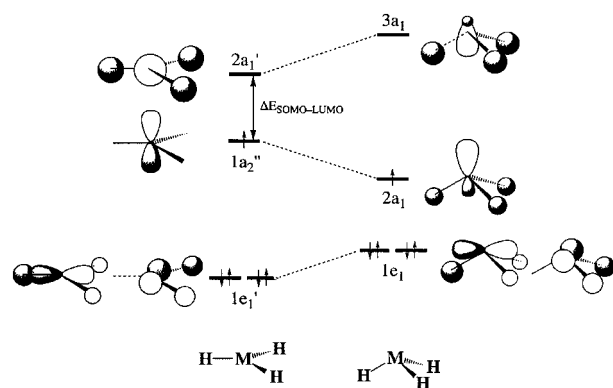
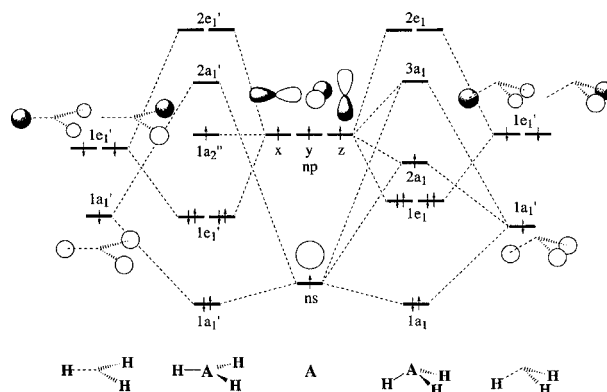**FIGURE 13.** Walsh diagram for the pyramidalization of $AH_3{}^{\bullet}$.

FIGURE 14. Schematic orbital interaction diagram for a planar (D_{3h}, left) and a pyramidal (C_{3v}, right) $AH_3{}^{\bullet}$ radical.

and the less A—H antibonding nature of the LUMO. The Jahn–Teller effect is opposed by the increasing energy of the $1e_1$ orbitals, which is ascribed to the loss of A—H bonding overlap. Thus, only $CH_3{}^{\bullet}$ remains planar because the Jahn–Teller effect is not strong enough in this case to outweigh the $1e_1$ destabilization. Thus, the emphasis in this traditional model is on the trend in electronic effects, i.e., bonding orbital interactions, that are not strong enough to pyramidalize $CH_3{}^{\bullet}$.

A careful Kohn–Sham MO analysis (at BP86/TZ2P) leads to a substantial revision of this picture. To understand the trends in pyramidalization of the four $AH_3{}^{\bullet}$ radicals, we have analyzed how the H—H and A—H interactions in $AH_3{}^{\bullet}$, $\Delta E_{int}(H_3)$ and $\Delta E_{int}(A—H_3)$, change if we go from the optimized planar structure to a pyramidal geometry. The A—H bond distance is kept fixed to its value in the planar radical. The H—A—H angle β is bent to its value in the optimized pyramidal structure (for $CH_3{}^{\bullet}$ the optimum H—A—H angle β of $SiH_3{}^{\bullet}$ was used, because there is no stationary point corresponding to a pyramidal methyl radical).

As shown in Figure 14 (to the left and the right), the H_3 fragment in $AH_3{}^{\bullet}$ has a $(1a_1')^1(1e_1')^2$ valence state, i.e., one electron in the bonding $1a_1$ combination of the three hydrogen 1s AOs and one electron in each of the degenerate antibonding $1e_1$ combinations. This gives rise to steric H—H repulsion that can be conceived as Pauli repulsion between three same-spin electrons. There is a striking difference between $CH_3{}^{\bullet}$ and the heavier homologs. In $CH_3{}^{\bullet}$ the H—H steric repulsion $\Delta E^0(H_3)$ and, hence, $\Delta E_{int}(H_3)$ is significantly stronger, and increases much more upon pyramidalization: the H—H interaction becomes more repulsive by 4.0 kcal/mol for $CH_3{}^{\bullet}$ and only by 1.1 kcal/mol or less for $SiH_3{}^{\bullet}$, $GeH_3{}^{\bullet}$, and $SnH_3{}^{\bullet}$. The reason is simply the shorter

A—H bond and H—H distance in $CH_3{}^{\bullet}$, which leads to a larger H—H $\langle 1s|1s \rangle$ overlap (0.32 compared to, e.g., 0.16 in $SiH_3{}^{\bullet}$). The H—H repulsion is slightly relieved and partly hidden when the A—H bond is allowed to adapt, by elongation, to the pyramidal geometry.

The A—H interaction is provided by the formation of three electron-pair bonds, one in A symmetry, and two degenerate ones in E symmetry, as shown in Figure 14. Only if $AH_3{}^{\bullet}$ is pyramidal (Fig. 14, to the right), the singly occupied np_z AO of the central atom can be stabilized by a bonding overlap with the $1a_1'$ orbital of the H_3 fragment. The bonding A—H orbital interactions in A symmetry hence favor pyramidalization. The overall A—H bonding interaction $\Delta E_{int}(A—H_3)$ is largest for $CH_3{}^{\bullet}$, but the additional stabilization $\Delta\Delta E_{int}(A—H_3)$ upon pyramidalization is the weakest, namely 0.4, −5.3, −4.7, and −6.3 kcal/mol along $CH_3{}^{\bullet}$, $SiH_3{}^{\bullet}$, $GeH_3{}^{\bullet}$, and $SnH_3{}^{\bullet}$. Note that the bonding orbital interactions in the methyl radical still favor pyramidalization, i.e., $\Delta\Delta E_{oi}(C—H_3) = -1.9$ kcal/mol; only the $\Delta\Delta E^0(C—H_3)$ contribution causes the overall change in C—H interaction to slightly disfavor a pyramidal methyl radical. The trend in $\Delta\Delta E_{int}(A—H_3)$ along A = C to Sn follows that of the increasing gain in A—H_3 overlap and stabilizing orbital interaction $\Delta\Delta E_A$ between the np_z AO of the central atom and the $1a_1'$ combination of the three hydrogen atom 1s AOs (i.e., 1s + 1s + 1s). The interactions in E symmetry are relatively insensitive to the pyramidalization process.

In conclusion, our Kohn–Sham MO approach shows that the $CH_3{}^{\bullet}$ radical is planar mainly because of the steric repulsion between the hydrogen ligands. The steric H—H repulsion is much weaker for the heavier central atom homologs in which the

ligands are farther removed from each other. Electronic effects (i.e., electron pair bonding between central atom and hydrogen ligands) always favor a pyramidal structure, although only slightly so for the methyl radical. As a result, there is an increasing degree of pyramidalization if we go from $CH_3{}^{\bullet}$ down to $SnH_3{}^{\bullet}$. This differs from the classical explanation for the trend in $AH_3{}^{\bullet}$ geometry and inversion barrier as sketched in the introduction of this section. The difference in interpretation is that the main opposing factor to pyramidalization, i.e., the reason why $1e_1$ MOs go up in energy in the Walsh diagram of Figure 13, is the increase in repulsive H—H $\langle 1s|1s \rangle$ overlap and not the loss in $\langle np_{xy}|1e_1' \rangle$ bonding overlap.

The preceding discussion illustrates the relevance of a quantitatively accurate description of the various terms in the interaction. It allows us, for instance, to accurately predict the geometry and the inversion barrier of $AH_3{}^{\bullet}$. It also yields the correct qualitative MO model that adequately accounts for the often-delicate balance of cooperating and counteracting mechanisms behind the observed trends.

HIGHLY POLAR ELECTRON-PAIR BONDING

In the Electron-Pair Bond section, we have analyzed electron pair bonding between equal fragments. But what happens if the difference in electronegativity becomes very large, such as in the strongly polar carbon–lithium bond.[113] The picture of the bond that has evolved from numerous *ab initio* studies is that of a predominantly ionic interaction (**J**, Fig. 15).[196–198] This is mainly based on the results of a number of advanced schemes for computing atomic charges. We mention the natural population analysis of Weinhold,[199–201] the integrated projected population (IPP) of Streitwieser,[202] and the atoms-in-molecules (AIM) approach of Bader.[203] They yield strongly positive lithium atomic charges ranging from $+0.75$ to $+0.90$ electrons.[204–208] Based on these numbers it was concluded that the C—Li bond is ionic, and that organolithium oligomers

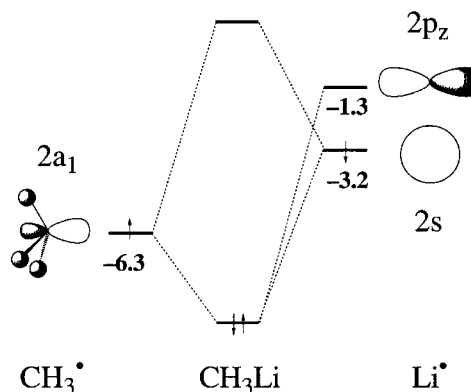**FIGURE 15.** Ionic (**J**) and covalent (**K**) representation of the C—Li bond.

FIGURE 16. Schematic orbital interaction diagram for CH_3Li (orbital energies in eV).

$(RLi)_n$ can be conceived as salt-like aggregates of lithium cations and carbanions, bound by electrostatic forces.

However, a detailed reexamination within the framework of Kohn–Sham MO theory leads to a principally different conception. The C—Li bond in CH_3Li may very well be envisaged as an electron-pair bond (**K**, Fig. 15), even though it is certainly polar. Our analysis is based on nonlocal DFT computations at the BP86/TZ2P level (see ref. 113 for computational details).

We begin with the C—Li bonding mechanism in monomeric methyllithium. This can be analyzed in two ways: (1) homolytically, as an interaction between $CH_3{}^{\bullet}$ and $Li^{\bullet}$—corresponding to a covalent view (**K**)—and (2) heterolytically, as an interaction between $CH_3{}^{-}$ and Li^{+}—this corresponds to an ionic view (**J**). It is instructive to compare the two approaches. We begin with the homolytic approach. The methyl $2a_1$-SOMO and the 3 eV higher energy lithium 2s-SOMO have a sizeable overlap of 0.33, and enter into a strongly polar electron pair bond (see Fig. 16) with substantial $2a_1 \pm 2s$ mixing. The latter, together with a sizeable admixture of lithium $2p_z$, is responsible for the covalent character of the C—Li bond. The increased population of the methyl $2a_1$ of 1.40 electrons reflects polarity. Note, however, that the lithium 2s still keeps a population of 0.50 and that the lithium $2p_z$ aequires a population of 0.19 electrons! Interestingly, the associated orbital interaction of -62.9 kcal/mol is twice as large as the classical electrostatic interaction ΔV_{elst} of only -32.1 kcal/mol. The overall homolytic bond enthalpy (for 298 K) amounts to -43.7 kcal/mol.

One might also analyze the interaction from an ionic or heterolytic point of view (**J**). Not

unexpectedly, due to the charge separation that occurs, this leads to an enormous increase in the electrostatic interaction ΔV_{elst} from -32.1 to -198.9 kcal/mol. However, this choice also implies that one pays a high price in terms of energy. The fragments have to be electronically excited by transferring an electron from lithium to methyl. Subsequently, more than half of this electron is transferred back to lithium through donor–acceptor interaction of -15 kcal/mol between the methyl $2a_1$ (now the lone-pair on CH_3^-) and the lithium $2s$ (LUMO of Li^+). After all, this translates into the heterolytic dissociation ($-\Delta E_{hetero} = 174.2$ kcal/mol) being four times more endothermic, i.e., less favorable, than the homolytic dissociation ($-\Delta E = 45.5$ kcal/mol). Furthermore, the heterolytic approach provides an unbalanced starting point for the oligomers: excessive electrostatic repulsion, especially between lithium cations (e.g., $+843$ kcal/mol for Li_4^{4+}), have to be compensated by even larger donor/acceptor and electrostatic interactions between the methyl anion cage and the lithium cation cluster. This does not provide a transparent description of C—Li bonding, and it also complicates understanding the cohesion within the central lithium cluster. On the basis of these and other arguments[113] we conclude that a homolytic approach is in many respects the more natural one.

Next, we discuss the C—Li bond in the methyllithium tetramer solely in terms of the homolytic approach. The computed overall bond energy ΔE for the formation of $(CH_3Li)_4$ from $4\ CH_3^{\bullet} + 4\ Li^{\bullet}$ is -308.6 kcal/mol and the methyllithium tetramerization energy is -126.6 kcal/mol. The carbon–lithium bond in $(CH_3—Li)_4$ is formed between an outer tetramethyl cage, $(CH_3^{\bullet})_4$ with $d_{CC} = 3.6$ Å, and an inner tetralithium cluster, $(Li^{\bullet})_4$ with $d_{Li,Li} = 2.4$ Å (see Fig. 17). These fragments have quintet electronic valence states with one electron in a C—C (or Li—Li) bonding orbital of A_1 symmetry and three electrons in a set of triply degenerate C—C (or Li—Li) antibonding orbitals of T_2 symmetry. These frontier orbitals stem from the interacting SOMOs of the respective monomeric fragments, i.e., methyl $2a_1$ and lithium $2s$ (Fig. 16). The tetramethyl fragment has a relatively small energy gap of 1.2 eV between the C—C bonding $2a_1$ and the C—C antibonding $3t_2$ SOMOs because the 4 methyl $2a_1$ SOMOs are quite far away from each other. In the inner cluster of lithium atoms, an interesting phenomenon occurs. Due to the enormous overlap of 0.65 between the Li $2s$ orbitals, the bonding $1a_1$ combination SOMO$_{low}$ is significantly stabilized, and this
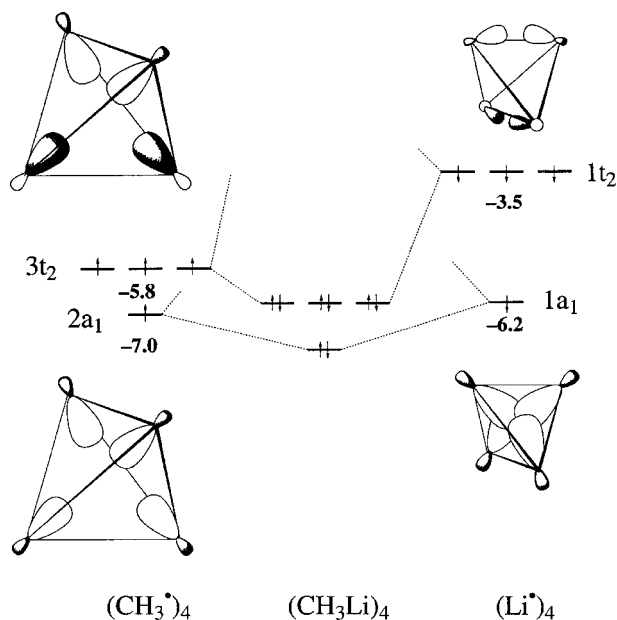

FIGURE 17. Schematic orbital interaction diagram for $(CH_3Li)_4$ (orbital energies in eV).

effect is further reinforced by a strong $2s$–$2p$ mixing. This has an important consequence for the C—Li electron pair bond $2a_1 + 1a_1$ occurring in the A_1 symmetry. The energy of the tetralithium $1a_1$ SOMO (-6.2 eV) is so much lowered with respect to that of the isolated-lithium $2s$ AO (-3.2 eV) that it begins to approach the energy of the $2a_1$ partner SOMO (-7.0 eV) on the more electronegative carbon fragment (Fig. 17). The electronegativity of lithium is effectively increased in the cluster as regards the interactions in the A_1 symmetry. This leads to a virtually covalent electron-pair bond in which the respective partner SOMOs more or less keep their original population of one electron! The $2a_1 + 1a_1$ electron-pair bond ($\Delta E_{A1} = -85.8$ kcal/mol) is also stronger than that in the methyllithium monomer ($\Delta E_{A1} = -62.9$ kcal/mol), among others, because of a more efficient overlap (0.55 compared to 0.33). The transfer of electrons out of the lithium cluster into the methyl cage is caused nearly exclusively by the three more polar $3t_2 + 1t_2$ electron-pair bonds in T_2 symmetry, which together contribute -387.0 kcal/mol to the carbon–lithium interaction. Note that this bonding mechanism does not only provide C—Li bonding, but also increases the cohesion within the Li_4 cluster! This is because there is a selective depopulation of the Li—Li antibonding $1t_2$ orbitals (which hold a population of only 0.65

electrons each) while the Li—Li bonding $1a_1$ orbital keeps its population.

Altogether, the Kohn–Sham MO analysis clearly shows that the polarity of the carbon–lithium bond decreases on oligomerization. This conclusion fully agrees with the trends we obtain from VDD and Hirshfeld analyses of the charge density distribution for the methyllithium monomer, dimer (left out in the discussion of the electronic structures) and tetramer. The VDD lithium charges are relatively small and they decrease from +0.38 via +0.26 to +0.13 electrons along CH_3Li, $(CH_3Li)_2$, and $(CH_3Li)_4$, showing that the shift of electron density from lithium to methyl decreases upon oligomerization. Whereas the values of the Hirshfeld lithium charges are somewhat larger, they display the same trend, again a decrease, namely from +0.49 via +0.42 down to +0.30 electrons along the same series. The NPA lithium charges of +0.85, +0.88 and +0.86 electrons ($MP4SDQ/6-31+G^*$) are significantly larger.[113] Strikingly, they are rather constant, and do not monitor the reduction of Li $\rightarrow$ CH_3 charge transfer upon oligomerization. We consider these three methods as well as other schemes (e.g., Bader's AIM) as satisfactory approaches for the computation of basis set independent and chemically meaningful atomic charges.[113, 116, 209] Yet, numerically, the methods yield rather different values for the atomic charges. This shows that atomic charges are no absolute quantities; they become meaningful only by comparing a trend along different molecules. The label "90% ionic" for the C—Li bond based on a computed lithium charge of +0.9 electrons is, therefore, not justified.

The VDD method has meanwhile been extended in two ways.[114, 119, 210] First, it can be used to study the *change* in atomic charges in polyatomic fragments caused by the chemical bond between these fragments, for example, if two methyl radicals combine to form ethane or two DNA bases associate to become a Watson–Crick pair. Apart from providing additional insight, this approach eliminates artefacts caused by the so-called front-atom problem that, in principle, all methods for computing atomic charges suffer from.[119] Second, the changes in atomic VDD charges that are caused by the chemical interactions can be decomposed into the contributions from different irreducible representations. This enables one, for example, to examine in a straightforward manner the charge redistribution in the σ and the π electron systems separately as long as they occur in different irreducible representations.[119, 210]

Chemical Reactivity

THE ACTIVATION STRAIN MODEL

In the previous sections we have focussed on bonding and structure. However, ADF is also highly suitable for tackling chemical reactions. The recently introduced[30] activation strain (or activation strain–TS interaction, ATS) model of chemical reactivity enables a transparent description and a detailed understanding of activation barriers and relative efficiencies of competing reaction mechanisms, and how they may be affected by modifying the reactants or reaction conditions (e.g., solvation). Basically, the activation strain–TS interaction (ATS) model evolves from a fragment approach (a key concept in ADF) to analyzing transition states and activation barriers. In the ATS model, the activation energy $\Delta E^{\neq}$ of a reaction is decomposed into two terms. The first is the activation strain $\Delta E^{\neq}_{strain}$, which is the energy necessary to deform the separate reactants to the geometry they adopt in the activated complex. The second, the TS interaction $\Delta E^{\neq}_{int}$, is the interaction energy between the deformed reactants in the transition state (TS). This is illustrated for an S_N2 reaction in Figure 18. The TS interaction $\Delta E^{\neq}_{int}$ between the strained reactants can be further decomposed, for example, into the classical electrostatic interaction, Pauli repulsive orbital interaction and bonding orbital interactions ($\Delta E^{\neq}_{int} = \Delta V_{elst} + \Delta E_{Pauli} + \Delta E_{oi}$) using the extended transition state (ETS) method developed by Ziegler and Rauk,[30, 211] in the same way as ΔE_{int} between fragments of a stable minimum energy structure (see the Bond Energy Analysis section). Note, however, that the activation strain (or ATS) model of chemical reactivity is, in principle, completely in-
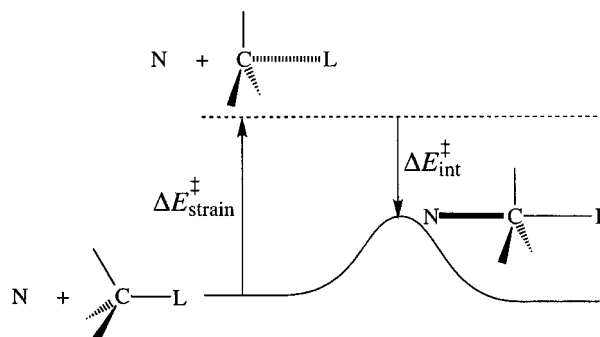

FIGURE 18. The activation strain–TS interaction (ATS) model of chemical reactivity.

dependent of any model or decomposition of the chemical bond as such.

The important point about the ATS concepts is that they provide intuitive and computable quantities that allow for a direct comparison of structurally unrelated and, in general, nonisolobal transition states. Although the model is not confined to DFT (it can equally well be applied in *ab initio* and semiempirical approaches), its combination with the Kohn–Sham MO theory and the ADF fragment approach leads to a particularly powerful interpretative tool. This can be applied, for example, to optimize a catalyst, that is, to minimize the activation barrier of the rate-determining step of the catalytic mechanism. This can be done by tuning the catalyst's electronic structure, by choosing suitable ligands, such that (for a given activation strain) the TS interaction with the substrate is maximized (see refs. 30 and 211 for applications to organometallic reactions and homogeneous catalysis). But the activation strain model is also useful for understanding and directing elementary organic reactions. In the following, we discuss two such examples: E2 elimination and S_N2 substitution.

ANTI- VS. SYN-ELIMINATION

Base-induced 1,2-elimination (E2, Fig. 19 upper branch) and nucleophilic substitution (S_N2, Fig. 19 lower branch) are two fundamental types of chemical reactions. In principle, E2 elimination is always in competition with S_N2 substitution, and the two pathways may occur as unwanted side reactions of each other. A thorough understanding of what determines these processes is important for the design of efficient syntheses.

In this section, we focus on the stereochemistry of E2 eliminations, and wonder why they proceed preferentially via a coplanar H^β—C^β—C^α—L arrangement of the substrate, and why the anti-elimination generally prevails over syn-elimination. We consider here the *anti*-E2 and *syn*-E2 pathways of the simple model reaction between a fluoride anion as base and fluoroethane as substrate (F^- + C_2H_5F, see Fig. 20). This has been investigated at the BVWN-Stol1/TZ2P//$X\alpha$/DZP level of theory.[30, 212]
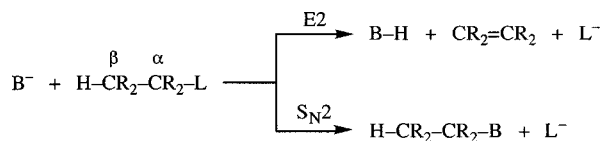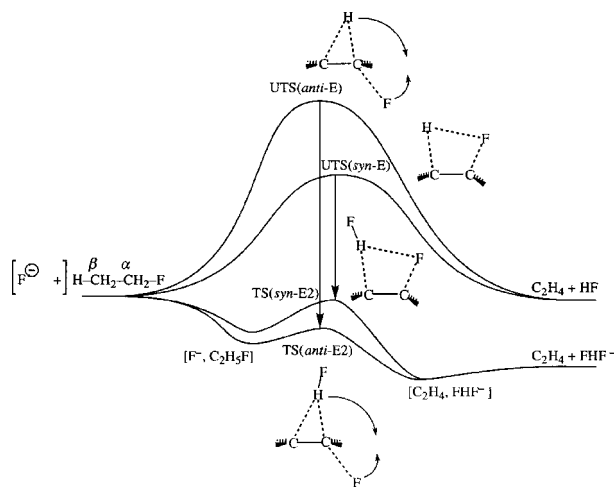

FIGURE 20. ATS approach to anti- vs. syn-E2 stereochemistry.

The conclusions of ref. 212 are confirmed by the preliminary results of recent BP86/TZ2P calculations.

The reactions proceed through abstraction of a β-proton by the base under formation of ethylene, the expelled leaving group F^-, and the conjugate acid HF. The latter two form a complex FHF^-, which makes the gas-phase reaction exothermic by -40.4 kcal/mol. The syn-E2 transition state ($\Delta E^{\neq} = -0.5$ kcal/mol) is 9 kcal/mol higher in energy than that for anti-E2 elimination ($\Delta E^{\neq} = -9.5$ kcal/mol); this is represented by the two lower energy pathways in Figure 20. A traditional and plausible explanation for this has been the increased repulsion associated with the eclipsed conformation of the substrate. But, this argument turns out to be erroneous. In the first place, eclipsed fluoroethane is only 2.3 kcal/mol higher in energy than the staggered conformer is; this does not account for the difference of 9 kcal/mol in activation energies. But, more importantly, it is the difference in energy between the deformed substrates in the respective *transition states* that counts in this context, and *not* the relative energy of the staggered and eclipsed conformers of the isolated fluoroethane reactant.

This brings us naturally to the concept of activation strain ($\Delta E^{\neq}_{\text{strain}}$). The *syn*-elimination reaches the TS at a point where the C_2H_5F substrate is much less deformed than in the *anti*-E2 transition state. This is simply due to the fact that in the *syn*-E2 TS the conjugate acid and the leaving group are located directly in front of each other. A slight internal rotation and a "moderate" elongation of the C^β—H and C^α—F bonds (by 39 and 11%, respectively, at
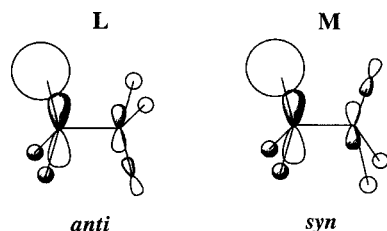

FIGURE 19. E2 elimination and S_N2 substitution.

L   **M**

anti   *syn*

FIGURE 21. Schematic representation of the LUMO of the CH_3CH_2F substrate in the *trans* (**L**) and *cis* (**M**) conformation that lead to anti- and *cis*-E2 elimination, respectively.

$X\alpha$/DZP) enable the abstracted proton and the leaving group to interact and stabilize the system. The energy does not rise any further, and the transition state is reached. Such a stabilizing interaction is not possible in an early stage of the *anti*-elimination, and the *anti*-E2 TS is reached somewhat later, after a much stronger elongation of the C^β—H and C^α—F bonds (by 67 and 51%). When we consider the "activation strain" in the substrate, i.e., the deformation energy associated with bringing C_2H_5F into the geometry of the TS, the *syn*-elimination with 83 kcal/mol should be the more favorable process and *not* the *anti*-elimination with 126 kcal/mol. The two higher energy pathways in Figure 20 reflect this (UTS refers to "uncatalyzed" TS, i.e., with the base removed). The "activation strain" may be conceived as a good estimate of the barrier for the corresponding thermal elimination (i.e., without the assistance of a base) of HF from fluoroethane which occurs indeed in a *syn*-fashion.[213, 214]

So it is the TS interaction $\Delta E_{int}^\#$ with the base that leads to the preference for *anti*-elimination. To understand this, we take a closer look at the substrate's LUMO, the acceptor orbital in the interaction with the HOMO of the base. It is the π-bonding combination between the lowest unoccupied e_x^* orbitals of the $CH_3^\bullet$ (left side of **L** and **M** in Fig. 21) and the $\cdot CH_2F$ fragments (right side of **L** and **M** in Fig. 21) that has C—H and C—F antibonding character (see also the Role of the Pauli Steric Repulsion section).[193]

Therefore, the antibonding character of the LUMO is reduced and it decreases in energy, as the C^β—H and C^α—F bonds elongate. This is the key to the answer of our question. The LUMO of the strongly deformed substrate *anti*-TS is much lower in energy, by 2.2 eV, than that in the *syn*-TS. It is, therefore, closer in energy to the HOMO of the base and enters into a significantly more stabilizing donor–acceptor interaction.[30, 212] This may be conceived as a textbook example of a catalytic process

where the base is a selective catalyst that favors the high-energy process (Fig. 20). However, one restriction applies to this analogy: the base is not recovered after elimination has taken place; the catalyst is poisoned, so to say, with a product molecule (HF), and is needed in stoichiometric amounts. The tendency to adopt a coplanar arrangement of the C^β—H and C^α—F bond, either *anti* or *syn*, can be understood on the basis of the C—C π-bonding character of the substrate LUMO. In that case, the π overlap is optimal leading to a low LUMO energy and thus a strong TS interaction with the base HOMO.

SUBSTITUTION VS. ELIMINATION

In this section, we examine how base-induced *anti*-elimination competes with nucleophilic S_N2 substitution and the influence of (micro)solvation.[30, 212, 215, 216] Figure 22 shows the respective reaction energy profiles for our model system F^- + C_2H_5F.

Starting from the same reactant complex (F^-, C_2H_5F) from which E2 elimination may proceed, the base can also move toward the backside of the α-methyl group and perform a symmetric and, therefore, thermoneutral nucleophilic substitution. The activation energy for S_N2 substitution (-0.5 kcal/mol) is again higher than that for E2 elimination (-9.5 kcal/mol, see Table I), in line with the experimental observation that (anionic) eliminations strongly dominate substitution in the gas phase.[217–224] On the other hand, it is well known that in the condensed phase, this relative order is reversed or, at least, shifted in favor of substitution,[225–227] and that the absolute rate of both processes decreases drastically, by up to 20 orders of magnitude.[228]
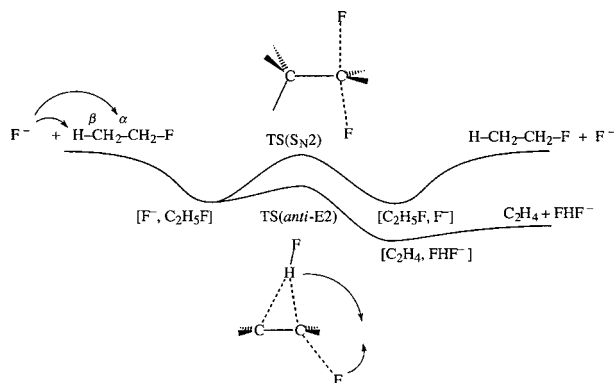

FIGURE 22. Reaction energy profiles for the S_N2 vs. E2 competition in the gas phase.

Activation Energies for E2 and S_N2 Reactions of $F^- + C_2H_5F$.[a]

Reaction	E2[b]	S_N2
Gas phase	−9.5	−0.5
Monosolvated base[c]	31.6	23.0
Disolvated base[c]	54.4	34.4

[a] In kcal/mol. BVWN-Stoll/TZ2P//$X\alpha$/DZP.
[b] *Anti*-elimination.
[c] With hydrogen fluoride model solvent molecules.

We have tried to model these solvent effects theoretically by microsolvation, that is, by introducing only one or two HF molecules as models for protic solvent molecules. Many solvation modes are conceivable.[216] Here, we examine the effect of mono- and disolvation of the F^- base. Surprisingly, already the introduction of one single HF solvent molecule causes a number of striking changes in the reaction energy profile: (1) The pronounced wells of the reactant and product complexes become very shallow, and (2) the activation energies that were negative are now becoming positive (Table I). The trend continues as the second solvent molecule is brought into play. This can be understood in terms of differential solvation of reactants—which are strongly stabilized—and transition states—which are weakly stabilized. Only one or two solvent molecules bring us from the double-well potential, typical for the gas phase, to a nearly unimodal reaction energy profile that is characteristic for reactions in the condensed phase. Of course, we are still far removed from a real condensed-phase reaction that takes place in bulk solvent. But this result shows that some very important effects occur in the first solvation shell. Interestingly, we also find the reversal of activation energies: on disolvation, for example, the S_N2 barrier is 20 kcal/mol lower than the E2 barrier (Table I).

Finally, we address the question *why* the intrinsic reactivity of $F^- + C_2H_5F$ is in favor of elimination and *why* this solvation shifts the reactivity toward substitution.[30] Again, following the ATS approach, we begin by inspecting the activation strain of the substrate in the *anti*-E2 and S_N2 transition states. As pointed out before, the *anti*-E2 transition state is strongly deformed, and much energy (126 kcal/mol) is needed to distort the substrate to the associated geometry. The S_N2 transition state, on the other hand, is much less deformed and tighter: a

new C^α—F bond is already being formed to quite an extent ($d_{CF} = 1.826$ Å), whereas the old one is elongated only moderately (by 26%). Accordingly, the activation strain of the substrate in TS(S_N2) is rather low, approximately 31 kcal/mol (see Fig. 23). Yet, the process is energetically unfavorable because of the significantly weaker and less stabilizing (donor–acceptor) TS interaction between the HOMO of the F^- nucleophile and the high-energy LUMO of the little deformed substrate.

Upon solvation, however, the F^- HOMO is stabilized (both by electrostatic and charge transfer interactions with the solvent molecules) resulting in an increase of the HOMO–LUMO gap and, therefore, a decrease of the TS interaction with the substrate LUMO. Whereas this HOMO–LUMO TS interaction as such remains still the strongest for the E2 transition state, the *weakening* in this stabilizing interaction on solvation of the base is, in absolute terms, the largest for this TS (Fig. 23). The high activation strain, a characteristic of the elimination process, makes the barrier of the solvated E2 elimination higher than that of the solvated S_N2 substitution (Fig. 23).

We stress the equivalence of this view on solvation effects and the one based on differential solvation. The ATS approach analyzes the interaction between base or nucleophile and the deformed substrate instead of that between solvent and reaction system. The advantage is that the same reasoning used for understanding the effect of solvation may also shed some light on the effect of varying the base itself. For example, assuming that other factors do
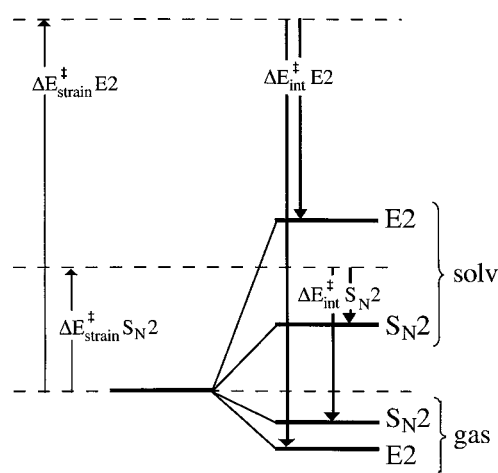

FIGURE 23. Activation strain ($\Delta E^{\#}_{strain}$) and TS interaction $\Delta E^{\#}_{int}$ in E2 and S_N2 transition states for an unsolvated (gas) and a solvated (solv) base.

not change and leaving out overlap considerations, it is easily seen that a stronger base—with a HOMO at high energy—tends to E2 elimination, whereas a weaker base—with a HOMO at low energy—inclines toward S_N2 substitution.

Structure and Bonding of DNA

Very recently, we have investigated the structure and nature of the deoxyribonucleic acid (DNA) molecule, making use of the linearization and parallelization of the ADF code.[119, 210, 229] The purpose has been to provide a foundation for an accurate, quantitative description of the structure and energetics of DNA, the influence of the molecular environment (such as, e.g., water molecules and counterions) and, in particular, a better understanding of the nature and behavior of this molecule that is of crucial importance for the existence of all life.

One of the key results (ref. 229, and references therein) is that we have unravelled a hitherto unresolved discrepancy between theoretical[230, 231] and experimental[232–234] hydrogen bond lengths in Watson–Crick base pairs. At first instance, we also arrive at the striking disagreement with experiment as shown in Figure 24 for the three hydrogen bonds in GC, for which we find a bond length pattern that is short-long-long (2.73, 2.88, and 2.87 Å, **3a**) at significant variance with the experimental values that

are long-long-short (2.91, 2.95, and 2.86 Å, **3d**). It appears that the disagreement is not due to an inadequacy of the quantum chemical method, in our case DFT at BP86 with the TZ2P basis (for which the BSSE is less than 1 kcal/mol). Instead, it is caused by a deficiency of the model systems used so far in theoretical computations (e.g., **3a** for GC), namely, the absence of the molecular environment (i.e., water, sugar OH groups, counterions) that the base pairs experience in the crystals studied experimentally. If we incorporate the major elements of this environment into our model, simulating them by water molecules and a Na^+ ion, we achieve excellent agreement with experiment at BP86/TZ2P (compare, for example, our **3c** with the experimental **3d**). Note that our best simulation of the environment includes all close contacts of the GC base pair with crystal water, sugar OH groups and counterions in the crystal. One may expect further improvements if a second or even higher order environment shells are introduced but the effects are likely to be much less pronounced than those of the first shell. On the other hand, whether plain nucleic bases (**3a**) or more realistic models for the nucleotides (**3b**) are used is much less important. This finding has an enormous scope because it shows that the already existing density functionals are capable of adequately describing biological molecules containing hydrogen bonds.
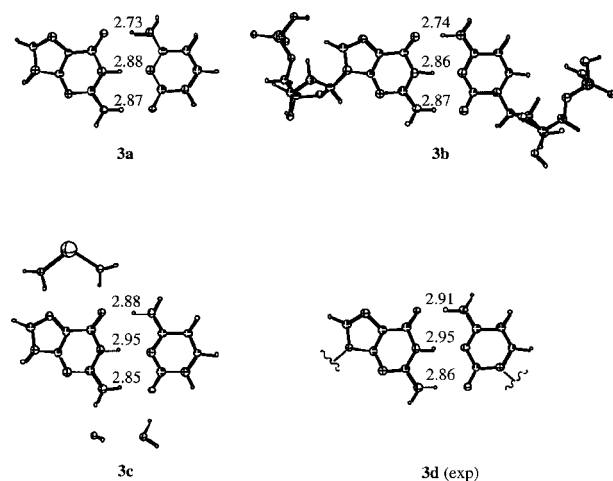

FIGURE 24. Hydrogen bond distances (in Å) in plain guanine–cytosine (GC, **3a**), GC with inclusion of the backbone (**3b**) and one of our GC model systems containing water molecules and a sodium counterion (**3c**) from BP86/TZ2P (**3a**, **3c**) and BP86/DZP (**3b**) computations and in the crystal of sodium guanylyl-3′,5′-cytidine nonahydrate from X-ray diffraction (**3d**).[234]

TDDFT: Absorption Spectrum of Porphin

The electronic absorption spectrum of the free base porphin (FBP) molecule has recently been studied by various *ab initio* methods. We have recently completed a similar study using the ADF-RESPONSE module[235] with satisfactory results, supporting the conclusion from a CASPT2 study (see ref. 236 and references therein). Our results for the most important low-lying excited states of this molecule are compared to experiment[237] in Table II.

The FBP molecule is interesting because there is an important role for interconfiguration mixing in the low-lying excitations, first described successfully at the semiempirical level by Gouterman[238] with his famous four-orbital model. This leads to the so-called B and Q bands in the FBP molecule as well as in other porphyrins. One can indeed observe the expected mixing by looking at the solution vectors of the excitation energy eigenvalue equation. In this way one sees the weight of various orbital replacements to a certain excitation. This can, furthermore,

TABLE II.

TDDFT (BP86/ALDA) and Experimental Excitation Energies (eV) and Oscillator Strengths (*f*) for Free Base Porphin (FBP).

State	TDDFT[a] Excitation Energy (eV)	TDDFT[a] Oscillator Strength *f*	Experiment[b] Excitation Energy	Experiment[b] Oscillator Strength
1 $^1B_{3u}$	2.16	0.01	1.98–2.02 (Q_x)	0.01
1 $^1B_{2u}$	2.29	0.0005	2.33–2.42 (Q_y)	0.06
2 $^1B_{3u}$	3.01	0.04	3.13–3.33 (B)	1.15
2 $^1B_{2u}$	2.98	0.1338		
3 $^1B_{2u}$	3.41	0.8962	3.65 (N)	<0.1
3 $^1B_{3u}$	3.47	0.7293		
4 $^1B_{3u}$	3.77	0.1688	4.25 (L)	~0.1
4 $^1B_{2u}$	3.76	0.1272		

[a] Ref. 235.
[b] Ref. 237 and other references in ref. 235.

be used to study differences between related systems. The effect of adding a metal in the centre of the porphyrin or the effect of using a different macrocycle immediately shows up in the positions of the excitation energies, the magnitude of the oscillator strengths, and, perhaps most interestingly, in the weights of the solution vectors. From such information, one can relate the positions and magnitudes of peaks in the absorption spectrum to the geometrical and electronic structure of the molecule. In this way, the ADF-RESPONSE module can help to understand differences between spectra of various molecules.

An important feature of the TDDFT results in Table II is the paired structure of the $^1B_{2u}$ and the $^1B_{3u}$ excitations. All low-lying experimental bands are assigned to a pair of $^1B_{2u}$ and $^1B_{3u}$ excitations, which is in full agreement with the CASPT2 results, and challenges previous coupled cluster and CI calculations.[239, 240]

Although the TDDFT excitation energies are a bit low with respect to experiment, the assignments are unambiguous. In the experimental spectrum, the B and N bands strongly overlap, so that one usually speaks of the B—N band system in FBP. The TDDFT results give large oscillator strengths in the N band. For metal porphyrins on the other hand, the TDDFT results agree with the experimental result that the B band is clearly separated from and much stronger than the N band. Therefore, the role that the B and N bands play in FBP differs substantially from the situation in closely related systems. Analysis of the TDDFT results can be a very useful aid in understanding such dif-

ferences. The research on the porphyrin spectra is ongoing, and also includes the nonlinar optical properties.[241]

Currently a fragment orbital analysis is being implemented to study the adsorption spectra of these and molecules in even greater detail.

Outlook

As we have discussed, ADF is a package for detailed and quantitative analysis of reactivity, structures, and various properties in the gas phase and in solution and for complicated and large-scale calculations on a large variety of systems. Being primarily academic software, ADF will continue to be developed as the result of ongoing scientific research. Focus and emphasis in code development naturally adjust to trends in scientific interests. This will target both functionality and performance. On a short-term further work on XC potentials and energy functionals, extension of the linear-scaling technology and improved parallelization behavior are at hand. With the systematic and rapid improvement of both hardware and software the applicability of ADF will cover more and more fields and increasingly more complex problems in chemistry, biology, and physics.

Online information about ADF, including user manuals, other documentation, and information about licenses and distribution, can be found at the internet address http://www.scm.com.

References

1. Parr, R. G.; Yang, W. Density-Functional Theory of Atoms and Molecules; Oxford University Press: New York, 1989.

2. Dreizler, R. M.; Gross, E. K. U. Density Functional Theory, an Approach to the Quantum Many-Body Problem; Springer Verlag: Berlin, 1990.

3. Ellis, D. E., Ed. Electronic Density Functional Theory of Molecules, Clusters and Solids; Kluwer Academic Publishers: Dordrecht, 1995.

4. Dunitz, J. D.; Hafner, K.; Houk, K. N.; Ito, S.; Lehn, J.-M.; Raymond, K. N.; Rees, C. W.; Thiem, J.; Vögtle, F., Eds. Topics in Current Chemistry; Springer: Berlin, 1996, vol. 183.

5. Seminario, J. M., Ed. Recent Developments and Applications of Modern Density Functional Theory; Elsevier: Amsterdam, 1996.

6. Baerends, E. J.; Ellis, D. E.; Ros, P. Chem Phys 1973, 2, 41.

7. Sambe, J.; Felton, R. H. J Chem Phys 1975, 62, 1122.

8. Ellis, D. E.; Adachi, H.; Averill, F. W. Surf Sci 1976, 58, 497.

9. Dunlap, B. I.; Corolly, J. W. P.; Sabin, J. R. J Chem Phys 1979, 71, 3396.

10. Delley, B.; Ellis, D. E. J Chem Phys 1982, 76, 1949.

11. (a) Boerrigter, P. M.; te Velde, G.; Baerends, E. J. Int J Quantum Chem 1988, 33, 87; (b) te Velde, G.; Baerends, E. J. J Comput Phys 1992, 99, 84.

12. te Velde, G.; Baerends, E. J. Phys Rev B 1991, 44, 7888.

13. Fonseca Guerra, C.; Visser, O.; Snijders, J. G.; te Velde, G.; Baerends, E. J. In Methods and Techniques in Computational Chemistry; Clementi, E.; Corongiu, G., Eds.; Stef: Cagliari, 1995, p. 305.

14. Andzelm, J. W.; Nguyen, D. T.; Eggenberger, R.; Salahub, D. R.; Hagler, A. T. Comput Chem 1995, 19, 145.

15. Fonseca Guerra, C.; Snijders, J. G.; te Velde, G.; Baerends, E. J. Theor Chem Acc 1998, 99, 391.

16. Ziegler, T. Chem Rev 1991, 91, 651.

17. Perdew, J. P.; Chevary, J. A.; Vosko, S. H.; Jackson, K. A.; Pederson, M. R.; Singh, D. J.; Fiolhais, C. Phys Rev B 1992, 46, 6671.

18. Becke, A. D. J Chem Phys 1992, 96, 2155.

19. Becke, A. D. J Chem Phys 1993, 98, 1372.

20. Becke, A. D. J Chem Phys 1993, 98, 5648.

21. Becke, A. D. J Chem Phys 1993, 97, 9173.

22. Ziegler, T. Can J Chem 1995, 73, 743.

23. Ziegler, T.; Rauk, A. Inorg Chem 1979, 18, 1558.

24. Ziegler, T.; Rauk, A. Inorg Chem 1979, 18, 1755.

25. Baerends, E. J.; Gritsenko, O. V.; van Leeuwen, R. In Chemical Applications in Density Functional Theory; Laird, B. B.; Ross, R. B.; Ziegler, T., Eds.; American Chemical Society: Washington, DC, 1996, p. 20.

26. Baerends, E. J.; Gritsenko, O. V.; van Leeuwen, R. In New Methods in Quantum Theory; Tsipis, C. A.; Popov, V. S.; Herschbach, D. R.; Avery, J. A., Eds.; Kluwer Academic Publishers: Dordrecht, 1996, vol. 8.

27. Baerends, E. J.; Gritsenko, O. V. J Phys Chem A 1997, 101, 5383.

28. Gritsenko, O. V.; Schipper, P. R. T.; Baerends, E. J. J Chem Phys 1997, 107, 5007.

29. Stowasser, R.; Hoffmann, R. J Am Chem Soc 1999, 121, 3414.

30. Bickelhaupt, F. M. J Comput Chem 1999, 20, 114.

31. Bickelhaupt, F. M.; Baerends, E. J. In Reviews of Computational Chemistry; Boyd, D. B.; Lipkowitz, K. B., Eds.; Wiley-VCH: New York, 2000, p. 1, vol. 15.

32. Redfern, P. C.; Blaudeau, J.-P.; Curtiss, L. A. J Phys Chem A 1997, 101, 8701.

33. Curtiss, L. A.; Redfern, P. C.; Raghavachari, K.; Pople, J. A. J Chem Phys 1998, 109, 42.

34. van Leeuwen, R.; Baerends, E. J. Phys Rev A 1994, 49, 2421.

35. Proynov, E. I.; Sirois, S.; Salahub, D. R. Int J Quantum Chem 1997, 64, 427.

36. Schipper, P. R. T.; Gritsenko, O. V.; Baerends, E. J. Phys Rev A 1998, 57, 1729.

37. van Voorhis, T.; Scuseria, G. E. J Chem Phys 1998, 109, 400.

38. Filatov, M.; Thiel, W. Phys Rev A 1998, 57, 189.

39. Krieger, J. B.; Chen, J.; Iafrate, G. J.; Savin, A. In Electron Correlations and Materials Properties; Gonis, A.; Kioussis, N., Eds.; Plenum: New York, 1999.

40. Perdew, J. P.; Kurth, S.; Zupan, A.; Blaha, P. Phys Rev Lett 1999, 82, 2544.

41. Perdew, J. P.; Kurth, S.; Zupan, A.; Blaha, P. Phys Rev Lett 1999, 82, 5179.

42. Tsuneda, T.; Suzumura, T.; Hirao, K. J Chem Phys 1999, 110, 10664.

43. Becke, A. D. J Chem Phys 2000, 112, 4020.

44. Boese, A. D.; Doltsinis, N. L.; Handy, N. C.; Sprik, M. J Chem Phys 2000, 112, 1670.

45. Proynov, E. I.; Chermette, H.; Salahub, D. R. J Chem Phys 2000, 113, 10013.

46. Boese, A. D.; Doltsinis, N. L.; Handy, N. C.; Sprik, M. J Chem Phys 2000, 112, 1670.

47. Rohklin, V. J Comput Phys 1985, 60, 187.

48. Greengard, L.; Rohklin, V. J Comput Phys 1987, 73, 325.

49. White, C. A.; Johnson, B. G.; Gill, P. M. W.; Head-Gordon, M. Chem Phys Lett 1994, 230, 8.

50. White, C. A.; Head-Gordon, M. J Chem Phys 1994, 101, 6593.

51. Strain, M. C.; Scuseria, G. E.; Frisch, M. J. Science 1995, 271, 51.

52. Kutteh, R.; Apra, E.; Nichols, J. Chem Phys Lett 1995, 238, 173.

53. Adamson, R. D.; Dombroski, J. P.; Taylor, S. W.; Gill, P. M. W. J Phys Chem 1996, 100, 6272.

54. Challacombe, M.; Schwegler, E.; Almlöf, J. J Chem Phys 1996, 104, 4685.

55. Gill, P. M. W. Chem Phys Lett 1997, 270, 193.

56. Schwegler, E.; Challacombe, M.; Head-Gordon, M. J Chem Phys 1997, 106, 5526.

57. Millam, J. M.; Scuseria, G. E. J Chem Phys 1997, 106, 5569.

58. Daniels, A. D.; Millam, J. M.; Scuseria, G. E. J Chem Phys 1997, 107, 425.

59. Stratman, R. E.; Scuseria, G. E.; Frisch, M. J. Chem Phys Lett 1997, 257, 213.

60. Kudin, K. N.; Scuseria, G. E. Chem Phys Lett 1998, 283, 61.

61. Kohn, W.; Sham, L. Phys Rev A 1965, 140, 1133.

62. Baerends, E. J.; Ros, P. Int J Quantum Chem 1978, S12, 169.

63. Snijders, J. G.; Baerends, E. J. Mol Phys 1978, 36, 1789.

64. Snijders, J. G.; Baerends, E. J.; Ros, P. Mol Phys 1979, 38, 1909.

65. van Lenthe, E.; Baerends, E. J.; Snijders, J. G. J Chem Phys 1993, 99, 4597.

66. van Lenthe, E.; Baerends, E. J.; Snijders, J. G. J Chem Phys 1994, 101, 9783.

67. van Gisbergen, S. J. A.; Snijders, J. G.; Baerends, E. J. J Chem Phys 1995, 103, 9347.

68. van Lenthe, E.; Snijders, J. G.; Baerends, E. J. J Chem Phys 1996, 105, 6505.

69. van Lenthe, E.; van Leeuwen, R.; Baerends, E. J.; Snijders, J. G. Int J Quantum Chem 1996, 57, 281.

70. van Gisbergen, S. J. A.; Osinga, V. P.; Gritsenko, O. V.; van Leeuwen, R.; Snijders, J. G.; Baerends, E. J. J Chem Phys 1996, 105, 3142.

71. van Gisbergen, S. J. A.; Snijders, J. G.; Baerends, E. J. J Chem Phys Lett 1996, 259, 599.

72. van Gisbergen, S. J. A.; Snijders, J. G.; Baerends, E. J. J Chem Phys 1998, 109, 10644.

73. van Gisbergen, S. J. A.; Snijders, J. G.; Baerends, E. J. J Chem Phys 1998, 109, 10657.

74. Versluis, L.; Ziegler, T. J Chem Phys 1988, 322, 88.

75. Fan, L.; Ziegler, T. J Chem Phys 1992, 96, 9005.

76. Deng, L.; Ziegler, T. Int J Quantum Chem 1994, 52, 731.

77. Schreckenbach, G.; Ziegler, T. J Phys Chem 1995, 99, 606.

78. Schreckenbach, G.; Ziegler, T. Int J Quantum Chem 1996, 60, 753.

79. Schreckenbach, G. Ph.D. thesis, University of Calgary, Calgary, 1996.

80. Schreckenbach, G.; Ziegler, T. Int J Quantum Chem 1997, 61, 899.

81. Wolff, S. K.; Ziegler, T. J Chem Phys 1998, 109, 895.

82. Wolff, S. K.; Ziegler, T.; van Lenthe, E.; Baerends, E. J. J Chem Phys 1999, 110, 7689.

83. Pye, C. C.; Ziegler, T. Theor Chem Acc 1999, 101, 396.

84. Woo, T. K.; Cavallo, L.; Ziegler, T. Theor Chem Acc 1998, 100, 307.

85. Woo, T. K.; Patchkovskii, S.; Ziegler, T. Comput Sci Eng 2000, 2, 28.

86. Philipsen, P. H. T.; van Lenthe, E.; Snijders, J. G.; Baerends, E. J. Phys Rev B 1997, 56, 13556.

87. Olsen, R. A.; Kroes, G. J.; Baerends, E. J. J Chem Phys 1999, 111, 11155.

88. Philipsen, P. H. T.; Baerends, E. J. Phys Rev B 2000, 61, 1773.

89. te Velde, G. Ph.D. thesis, Vrije Universiteit, Amsterdam, 1990.

90. van Lenthe, E.; Ehlers, A. E.; Baerends, E. J. J Chem Phys 1999, 110, 8943.

91. Raffenetti, R. C. J Chem Phys 1973, 59, 5936.

92. Pulay, P. Chem Phys Lett 1980, 73, 393.

93. Pulay, P. J Comput Chem 1982, 3, 556.

94. Hamilton, T. P.; Pulay, P. J Chem Phys 1986, 84, 5728.

95. Fischer, T. H.; Almlöf, J. J Phys Chem 1992, 96, 9768.

96. Burant, J. C.; Strain, M. C.; Scuseria, G. E.; Frisch, M. J. Chem Phys Lett 1996, 248, 43.

97. Warshel, A.; Levitt, M. J Mol Biol 1976, 103, 227.

98. Cornell, W. D.; Cieplak, P.; Bayly, C. I.; Gould, I. R.; Merz, K. M.; Ferguson, D. M.; Spellmeyer, D. C.; Fox, T.; Coldwell, J. W.; Kollman, P. A. J Am Chem Soc 1995, 117, 5179.

99. Rappe, A. K.; Casewit, C. J.; Colwell, K. S.; Skiff, W. M. J Am Chem Soc 1992, 114, 10024.

100. Singh, U. C.; Kollman, P. A. J Comput Chem 1986, 7, 718.

101. Maseras, F.; Morokuma, K. J Comput Chem 1995, 16, 1170.

102. Woo, T. K.; Margl, P. M.; Blöchl, P. E.; Ziegler, T. J Phys Chem B 1997, 101, 7877.

103. Cavallo, L.; Woo, T. K.; Ziegler, T. Can J Chem 1998, 76, 1457.

104. Deng, L.; Woo, T. K.; Cavallo, L.; Margl, P.; Ziegler, T. J Am Chem Soc 1997, 119, 6177.

105. Deng, L.; Ziegler, T.; Woo, T. K.; Margl, P.; Fan, L. Organometallics 1998, 17, 3240.

106. van Gisbergen, S. J. A.; Fonseca Guerra, C.; Baerends, E. J. J Comput Chem 2000, 21, 1511.

107. Hoffmann, R. Angew Chem Int Ed 1982, 21, 711.

108. Baerends, E. J.; Branchadell, V.; Sodupe, M. Chem Phys Lett 1997, 265, 481.

109. Morokuma, K. J Chem Phys 1971, 55, 1236.

110. Kitaura, K.; Morokuma, K. Int J Quantum Chem 1976, 10, 325.

111. Baerends, E. J. In Cluster Models for Surface and Bulk Phenomena; Nato Asi Series B; Pacchioni, G.; Bagus, P. S.; Parmigiani, F., Eds.; 1992, p. 189, vol. 283.

112. Ziegler, T.; Rauk, A. Theoret Chim Acta 1977, 46, 1.

113. Bickelhaupt, F. M.; van Eikema Hommes, N. J. R.; Fonseca Guerra, C.; Baerends, E. J. Organometallics 1996, 15, 2923.

114. Bickelhaupt, F. M.; Fonseca Guerra, C.; Handgraaf, J. W.; Baerends, E. J., in preparation.

115. Hirshfeld, F. L. Theoret Chim Acta 1977, 44, 129.

116. Wiberg, K. B.; Rablen, R. B. J Comput Chem 1993, 14, 1504.

117. Mulliken, R. S. J Chem Phys 1955, 23, 1833.

118. Mulliken, R. S. J Chem Phys 1955, 23, 2343.

119. Fonseca Guerra, C.; Bickelhaupt, F. M.; Snijders, J. G.; Baerends, E. J. Chem Eur J 1999, 5, 3581.

120. Ceperley, D. M.; Alder, B. J. Phys Rev Lett 1980, 45, 566.

121. Vosko, S. H.; Wilk, L.; Nusair, M. Can J Phys 1980, 58, 1200.

122. Stoll, H.; Pavlidou, C. M. E.; Preuss, H. Theoret Chim Acta 1978, 49, 143.

123. Perdew, J. P.; Wang, Y. Phys Rev B 1986, 33, 8800.

124. Perdew, J. P. Phys Rev B 1986, 33, 8822.

125. Becke, A. D. Phys Rev A 1988, 38, 3098.

126. Lee, C.; Yang, W.; Parr, R. G. Phys Rev B 1988, 37, 785.

127. Gritsenko, O. V.; Schipper, P. R. T.; Baerends, E. J. Chem Phys Lett 1999, 302, 199.

128. Schipper, P. R. T.; Gritsenko, O. V.; van Gisbergen, S. J. A.; Baerends, E. J. J Comput Phys 2000, 112, 1344.

129. Grüning, M.; Gritsenko, O. V.; van Gisbergen, S. J. A.; Baerends, E. J. J Chem Phys 2001, 114, 652.

130. Ziegler, T.; Snijders, J. G.; Baerends, E. J. J Chem Phys 1981, 74, 1271.

131. DeKock, R. L.; Baerends, E. J.; Boerrigter, P. M.; Snijders, J. G. Chem Phys Lett 1984, 105, 308.

132. DeKock, R. L.; Baerends, E. J.; Boerrigter, P. M.; Hengelmolen, R. J Am Chem Soc 1984, 106, 33387.

133. Boerrigter, P. M. Ph.D. thesis, Vrije Universiteit, Amsterdam, 1987.

134. Boerrigter, P. M.; Buijse, M. A.; Snijders, J. G. Chem Phys 1987, 111, 47.

135. Boerrigter, P. M.; Baerends, E. J.; Snijders, J. G. Chem Phys 1988, 122, 357.

136. Ziegler, T.; Tschinke, V.; Baerends, E. J.; Snijders, J. G.; Ravenek, W. J Phys Chem 1989, 93, 3050.

137. Li, J.; Scnreckenbach, G.; Ziegler, T. J Am Chem Soc 1995, 117, 486.

138. Bersuker, I. B.; Budnikov, S. S.; Leizerov, B. A. Int J Quantum Chem 1977, 11, 543.

139. Pascual-Ahuir, J. L.; Silla, E.; Tomasi, J.; Bonaccorsi, R. J Comput Chem 1987, 8, 778.

140. Klamt, A.; Schüürmann, G. J Chem Soc Perkin Trans 1993, 2, 799.

141. Klamt, A. J Phys Chem 1995, 99, 2224.

142. Pascual-Ahuir, J. L.; Silla, E. J Comput Chem 1990, 11, 1047.

143. Silla, E.; Tunón, L.; Pascual-Ahuir, J. L. J Comput Chem 1991, 12, 1077.

144. Versluis, L. Ph.D. thesis, University of Calgary, 1989.

145. Fan, L.; Ziegler, T. J Chem Phys 1991, 95, 7401.

146. Fan, L.; Versluis, L.; Ziegler, T.; Baerends, E. J.; Ravenek, W. Int J Quantum Chem Symp 1988, S22, 173.

147. Broyden, C. G. J Inst Math Applic 1970, 6, 76.

148. Fan, L.; Ziegler, T. J Am Chem Soc 1992, 114, 10890.

149. Gonzalez, C.; Schlegel, H. B. J Phys Chem 1990, 94, 5523.

150. Deng, L.; Ziegler, T. J Chem Phys 1993, 99, 3823.

151. Fukui, K. Acc Chem Res 1981, 14, 363.

152. Kraka, E.; Dunning, T. H., Jr. In Advances in Molecular Electronic Structure Theory; Dunning, T. H., Jr., Ed.; JAI Press: Greenwich, CT, 1990, vol. 1.

153. Fan, L.; Ziegler, T. J Phys Chem 1992, 96, 6937.

154. Torrent, M.; Gili, P.; Duran, M.; Sola, M. J Chem Phys 1996, 104, 9499.

155. Bérces, A.; Dickson, R. M.; Fan, L.; Jacobsen, H.; Swerhone, D.; Ziegler, T. Comput Phys Commun 1997, 100, 247.

156. Jacobsen, H.; Bérces, A.; Swerhone, D. P.; Ziegler, T. Comput Phys Commun 1997, 100, 263.

157. Schreckenbach, G.; Ziegler, T. Theor Chem Acc 1998, 99, 71.

158. Ruiz-Morales, Y.; Ziegler, T. J Phys Chem A 1998, 102, 3970.

159. Ruiz-Morales, Y.; Schreckenbach, G.; Ziegler, T. J Phys Chem 1997, 101, 4121.

160. Ruiz-Morales, Y.; Schreckenbach, G.; Ziegler, T. Organometallics 1996, 15, 3920.

161. Ruiz-Morales, Y.; Schreckenbach, G.; Ziegler, T. J Phys Chem 1996, 100, 3359.

162. Schreckenbach, G.; Ruiz-Morales, Y.; Ziegler, T. J Chem Phys 1996, 104, 8605.

163. Ehlers, A. W.; Ruiz-Morales, Y.; Baerends, E. J.; Ziegler, T. Inorg Chem 1997, 36, 5031.

164. Dickson, R. M.; Ziegler, T. J Phys Chem 1996, 100, 5286.

165. Khandogin, J.; Ziegler, T. Spectr Acta A 1999, 55, 607.

166. Khandogin, J.; Ziegler, T. J Phys Chem A 2000, 104, 113.

167. Autschbach, J.; Ziegler, T. J Chem Phys 2000, 113, 936.

168. Schreckenbach, G.; Ziegler, T. J Phys Chem A 1997, 101, 3388.

169. van Lenthe, E.; van der Avoird, A.; Wormer, P. E. S. J Chem Phys 1997, 107, 2488.

170. van Lenthe, E.; van der Avoird, A.; Wormer, P. E. S. J Chem Phys 1998, 108, 4783.

171. van Lenthe, E.; van der Avoird, A.; Hagen, W. R.; Reijerse, E. J Phys Chem A 2000, 104, 2070.

172. van Lenthe, E.; Baerends, E. J. J Chem Phys 2000, 112, 8279.

173. Gross, E. K. U.; Dobson, J. F.; Petersilka, M. In Density Functional Theory; Nalewajski, R. F., Ed.; Springer: Heidelberg, 1996.

174. van Gisbergen, S. J. A. Ph.D. thesis, Vrije Universiteit, Amsterdam, 1998.

175. van Gisbergen, S. J. A.; Snijders, J. G.; Baerends, E. J. Comput Phys Commun 1999, 118, 119.

176. van Gisbergen, S. J. A.; Kootstra, F.; Schipper, P. R. T.; Gritsenko, O. V.; Snijders, J. G.; Baerends, E. J. Phys Rev A 1998, 57, 2556.

177. Osinga, V. P.; van Gisbergen, S. J. A.; Snijders, J. G.; Baerends, E. J. J Chem Phys 1997, 106, 5091.

178. Casida, M. E. In Recent Advances in Density-Functional Methods; Chong, D. P., Ed.; World Scientific: Singapore, 1995, p. 155.

179. Bauernschmitt, R.; Ahlrichs, R. Chem Phys Lett 1996, 256, 454.

180. van Gisbergen, S. J. A.; Snijders, J. G.; Baerends, E. J. Phys Rev Lett 1997, 78, 3097.

181. Rosa, A.; Baerends, E. J.; van Gisbergen, S. J. A.; van Lenthe, E.; Groeneveld, J. A.; Snijders, J. G. J Am Chem Soc 1999, 121, 10356.

182. Bickelhaupt, F. M.; Nibbering, N. M. M.; van Wezenbeek, E. M.; Baerends, E. J. J Phys Chem 1992, 96, 4864.

183. Bickelhaupt, F. M.; Bickelhaupt, F. Chem Eur J 1999, 96, 4864.

184. Bickelhaupt, F. M.; Diefenbach, A.; de Visser, S. V.; de Koning, L. J.; Nibbering, N. M. M. J Phys Chem A 1998, 102, 9549.

185. Clark, T. J. J Am Chem Soc 1988, 110, 1672.

186. Gill, P. M. W.; Radom, L. J. J Am Chem Soc 1988, 110, 4931.

187. de Visser, S. V.; de Koning, L. J.; Nibbering, N. M. M. Int J Mass Spectrom Ion Processes 1996, 157/158, 283.

188. de Visser, S. V.; Bickelhaupt, F. M.; de Koning, L. J.; Nibbering, N. M. M. Int J Mass Spectrom Ion Processes 1998, 179/180, 43.

189. James, M. A.; McKee, M. L.; Illies, A. J. J J Am Chem Soc 1996, 118, 7836.

190. Deng, Y.; Illies, A. J.; James, M. A.; McKee, M. L.; Peschke, M. J. J Am Chem Soc 1995, 117, 420.

191. Sodupe, M.; Bertran, J.; Rodríguez-Santiago, L.; Baerends, E. J. J Phys Chem A 1999, 103, 166.

192. Noodleman, L.; Post, D.; Baerends, E. J. Chem Phys 1982, 64, 159.

193. Bickelhaupt, F. M.; Ziegler, T.; von Ragué Schleyer, P. Organometallics 1996, 15, 1477.

194. Albright, T. A.; Burdett, J. K.; Whangbo, M.-H., Orbital Interactions in Chemistry; Wiley–Interscience: New York, 1985.

195. Gimarc, B. M. Molecular Structure and Bonding; Academic Press: New York, 1979.

196. Streitwieser, A., Jr.; Bachrach, S. M.; Dorigo, A. E.; von Ragué Schleyer, P. In Lithium Chemistry; Sapse, A. M.; von Ragué Schleyer, P., Eds.; Wiley & Sons: New York, 1995.

197. Lambert, C.; von Ragué Schleyer, P. In Carbanionen. Methoden der Organischen Chemie (Houben-Weyl); Hanack, M., Ed.; Thieme: Stuttgart, 1993, vol. E19d.

198. Lambert, C.; von Ragué Schleyer, P. Angew Chem 1994, 106, 1187.

199. Reed, A. E.; Weinstock, R. B.; Weinhold, F. J Chem Phys 1985, 83, 735.

200. Reed, A. E.; Curtiss, L. A.; Weinhold, F. Chem Rev 1988, 88, 899.

201. Reed, A. E.; von Ragué Schleyer, P. J Am Chem Soc 1990, 112, 1434.

202. Collins, J. B.; Streitwieser, A., Jr. J Comput Chem 1980, 1, 81.

203. Bader, R. W. F. Atoms in Molecules, a Quantum Theory; Clarendon Press: Oxford, 1990.

204. Streitwieser, A., Jr.; Williams, J. W.; Alexandratos, S.; McKelvey, J. M. J Am Chem Soc 1976, 98, 4778.

205. Ritchie, J. P.; Bachrach, S. M. J Am Chem Soc 1987, 109, 5909.

206. Hiberty, P. C.; Cooper, D. L. J Mol Struct (Theochem) 1988, 169, 437.

207. Cioslowski, J. J Am Chem Soc 1989, 111, 8333.

208. Kaufmann, E.; Raghavachari, K.; Reed, A. E.; von Ragué Schleyer, P. Organometallics 1988, 7, 1597.

209. Meister, J.; Schwarz, W. H. E. J Phys Chem 1994, 98, 8245.

210. Fonseca Guerra, C.; Bickelhaupt, F. M. Angew Chem 1999, 111, 3120; Angew Chem Int Ed 1999, 38, 2942.

211. Bickelhaupt, F. M.; Ziegler, T.; von Ragué Schleyer, P. Organometallics 1995, 14, 2288.

212. Bickelhaupt, F. M.; Baerends, E. J.; Nibbering, N. M. M.; Ziegler, T. J Am Chem Soc 1993, 115, 9160.

213. Ferguson, H. A.; Ferguson, J. D.; Holmes, B. E. J Phys Chem 1998, 102, 5393.

214. Kato, S.; Morokuma, K. J Chem Phys 1980, 73, 3900.

215. Bertran, J. In New Theoretical Concepts for Understanding Organic Reactions; Bertran, J.; Csizmadia, I. G., Eds.; Kluwer Academic Publishers: Dordrecht, 1989, p. 231.

216. Bickelhaupt, F. M.; Baerends, E. J.; Nibbering, N. M. M. Chem Eur J 1996, 2, 196.

217. Nibbering, N. M. M. Acc Chem Res 1990, 23, 279.

218. Bickelhaupt, F. M.; Buisman, G. J. H.; de Koning, L. J.; Nibbering, N. M. M.; Baerends, E. J. J Am Chem Soc 1995, 117, 9889.

219. Bickelhaupt, F. M.; de Koning, L. J.; Nibbering, N. M. M. J Org Chem 1993, 58, 2436.

220. DeThuri, V. F.; Hintz, P. A.; Ervin, K. M. J Phys Chem A 1997, 101, 5969.

221. Li, C.; Ross, P.; Szulejko, J. E.; McMahon, T. B. J Am Chem Soc 1996, 118, 9360.

222. Lum, R. C.; Grabowski, J. J. J Am Chem Soc 1992, 114, 9663.

223. DePuy, C. H.; Gronert, S.; Mullin, A.; Bierbaum, V. M. J Am Chem Soc 1990, 112, 8650.

224. Jones, M. E.; Ellison, G. B. J Am Chem Soc 1989, 111, 1645.

225. March, J. Advanced Organic Chemistry; Wiley-Interscience: New York, 1997, 4th ed.

226. Reichardt, C. Solvents and Solvent Effects in Organic Chemistry; VCH: Weinheim, 1988, 2nd ed.

227. Isaacs, N. S. Physical Organic Chemistry; Longman: Harlow, 1995, 2nd ed.

228. Riveros, J. M.; José, S. M.; Takashima, K. Adv Phys Org Chem 1985, 21, 197.

229. Fonseca Guerra, C.; Bickelhaupt, F. M.; Snijders, J. G.; Baerends, E. J. J Am Chem Soc 2000, 122, 4117.

230. Bertran, J.; Oliva, A.; Rodríguez-Santiago, L.; Sodupe, M. J Am Chem Soc 1998, 120, 8159.

231. (a) Sponer, J.; Leszczynski, J.; Hobza, P. J Phys Chem 1996, 100, 1965; (b) Brameld, K.; Dasgupta, S.; Goddard, W. A., III. J Phys Chem 1997, 101, 4851.

232. Saenger, W. Principles of Nucleic Acid Structure; Springer Verlag: New York, 1984.

233. Seeman, N. C.; Rosenberg, J. M.; Suddath, F. L.; Kirn, J. J. P.; Rich, A. J Mol Biol 1976, 104, 109.

234. Rosenberg, J. M.; Seeman, N. C.; Day, R. O.; Rich, A. J Mol Biol 1976, 104, 145.

235. van Gisbergen, S. J. A.; Rosa, A.; Ricciardi, G.; Baerends, E. J. J Chem Phys 1999, 111, 2499.

236. Serrano-Andrés, L.; Merchán, M.; Rubio, M.; Roos, B. O. Chem Phys Lett 1998, 295, 195.

237. Edwards, L.; Dolphin, D. H.; Gouterman, M.; Adler, A. D. J Mol Spectr 1971, 38, 16.

238. Gouterman, M. J Mol Spectr 1961, 6, 138.

239. Gwaltney, S. R.; Bartlett, R. J. J Chem Phys 1998, 108, 6790.

240. Tokita, Y.; Hasegawa, J.; Nakatsuji, H. J Phys Chem A 1998, 102, 1843.

241. Ricciardi, G.; Rosa, A.; van Gisbergen, S. J. A.; Baerends, E. J. J Phys Chem A 2000, 104, 635.